Journal of Computational Physics **153,** 437–466 (1999)
Article ID jcph.1999.6285, available online at http://www.idealibrary.com on IDEAL®

MHD-A: A Fluctuation Splitting Wave Model for Planar Magnetohydrodynamics

Necdet Aslan

Physics Department, Yeditepe University, Üsküdar, 81130 İstanbul, Turkey
E-mail: necdet@yeditepe.edu.tr; necdet@alpha.nukleer.gov.tr

Received February 23, 1998; revised March 19, 1999

This paper describes a two-dimensional (2D) upwind residual distribution or fluctuation splitting (FS) scheme (MHD-A) for the numerical solutions of planar magnetohydrodynamics (MHD) equations on structured or unstructured triangular meshes. The scheme is second order in space and time, and utilizes a consistent 2D wave model originating from the eigensystem of a 2D jacobian matrix of the MHD flux vector. The possible waves existing in this wave model are entropy, magnetoacoustic, and (numerical) magnetic monopole waves; however, Alfven waves do not exist since the problem is planar.

One of the important features of the method is that the mesh structure has no influence on propagation directions of the waves. These directions are dependent only on flow properties and field gradients (for example, it is shown that the magnetoacoustic waves propagate in the directions of maximum and minimum magnetic strain rates). The other feature is that no flux evaluations and no information from the neighboring cells are needed to obtain a second order, positive, and linearity preserving scheme.

A variety of numerical tests carried out by the model on structured and unstructured triangular meshes show that MHD-A produces rather encouraging numerical results even though it is the first FS wave model ever developed for multidimensional MHD. © 1999 Academic Press

1. INTRODUCTION

Conservative, finite difference and finite volume schemes based on higher order Godunov methods have been effectively used to compute the solutions of hyperbolic systems of conservative laws [2–5]. Recently, Brio and Wu [6], Zachary and Colella [7], and Dai and Woodward [8] contributed to the early development of such upwind schemes to solve the magnetohydrodynamics (MHD) equations. Finite volume-type solvers were developed in two dimensions (2D) by Aslan [9–13], by Zachary *et al.* [7], by Powell *et al.* [14, 15], by Tanaka [36], by Roe *et al.* [16], and recently by Ryu *et al.* [17] and by Falle *et al.* [34].

0021-9991/99 $30.00
Copyright © 1999 by Academic Press
All rights of reproduction in any form reserved.

Most of these schemes were based on evaluating the numerical fluxes across the boundaries between cells as a function of left and right states. This paper deals with an alternative numerical method called the fluctuation splitting (FS) scheme and presents, for MHD, a multidimensional FS wave model first introduced by Aslan [18]. The model presented here includes a pair of fast and slow magnetoacoustic waves, an entropy (contact) wave, and a recently introduced [1] magnetic monopole wave to reduce the numerical problems due to the divergence condition (i.e., $\vec{\nabla} \cdot \mathbf{B} = 0$). This is an auxiliary condition introduced by Maxwell's equations, and a consistent and convergent discretization of the MHD equations is dependent on how it is satisfied numerically. A local nonzero divergence of magnetic field indicates the existence of magnetic monopoles within the cell, which suggests nonconservation of the magnetic flux across its surface. If no action is taken, this error grows during the computations, causing an artificial force parallel to the magnetic field (through the momentum equation), and destroys the correct dynamics of the flow [19].

One way to handle the nonphysical consequences of nonzero divergence is to employ a nonconservative form of MHD equations, as done by Brackbill and Barnes [19]. This method is unsatisfactory for flows containing strong shocks and discontinuities. Another way is to solve a Poisson equation for a scalar potential and correct the magnetic field with it to eliminate the spurious forces along the magnetic field (see Hujeirat [35] and references therein). This method is quite expensive and introduces difficulties during the differentiation of the scalar potential to correct the magnetic field. Furthermore, it was shown by Tanaka [36] that for some cases, an artificial divergence wave should be used along with the Poisson equation to obtain stabilization. Another way is to use stagerred grid approach in which the scalar quantities are placed at the center while the vector fields are considered at the cell edges (see Evans and Hawley [32]) in order to consistently discretize Faraday's law to eliminate the commutation error of the divergence and curl operators. The improvement obtained with this method (comparing with others) is that the maximum divergence constraint error reduces and remains constant at a lower value during the time evolution.

For the conservative form of MHD equations, the possibility of eliminating such numerical problems by means of a numerical magnetic monopole wave was first suggested by Aslan [1]. Although no numerical results were presented, Aslan observed that the slight modification of Faraday's law did not change the MHD wave structure but introduced a new divergence wave in the eigensystem as well as a monopole current source (i.e., $\mathbf{V}\vec{\nabla} \cdot \mathbf{B}$) in Faraday's law (see also Aslan *et al.* [9, 10]). Why a divergence source should be introduced into Faraday's law to compensate the nonphysical motions of numerical magnetic monopoles (arising from the discretization errors in the magnetic field) can be explained by carefully analysing Maxwell's equations for the electric field within moving and stationary frames (for details see the book by Jackson [20, Section. 6.1]). It is straighforward to show that using Ampere's law in conservative momentum equation also introduces a source related to $\mathbf{B}\vec{\nabla} \cdot \mathbf{B}$. Unless this source is identically zero, a spurious Lorentz force in the direction of magnetic field [19] will be created.

After Aslan introduced the idea of employing such a divergence source and nonopole wave in 1993, Powell [14] and Gombosi *et al.* [15] applied this idea to the solution of multidimensional MHD equations in 1994. Aslan's idea worked rather well, mostly eliminating the discretization errors due to the nonzero divergence of the magnetic field. After observing that his idea was working as well as that of Evans and Hawley [32], Aslan *et al.* [9] then succesfully employed the numerical magnetic monopole wave within a Riemann solver

(on quadrilateral grids) for the simulation of Tokamak-type plasmas, high beta (i.e., kinetic pressure > magnetic pressure) explosions, and subsonic and supersonic flows [9, 13]. Numerical results showed that this finite volume method produced impressive results for compressible flows, although it caused bifurcations and spurious oscillations for subsonic flows. The spurious oscillations produced by the wave models used in FS schemes for subsonic Eulerian flows were extensively discussed by Mesaros [21], who employed a hyperbolic–elliptic splitting scheme. Currently, the extension of this scheme for the subsonic MHD equations is being investigated by the author.

It is important to understand that the FS scheme presented here utilizes no fluxes since the modified jacobian matrices are not jacobian of any flux; thus, the present method differs from that developed by Powell [14], who utilized the fluxes and divergence source explicitly. Although the present method is developed to account for a divergence source, numerical results showed that the source has only a minor effect and it can be neglected. The good feature of the FS scheme presented here is that for all the test problems, solved on structured or even highly distorted unstructured meshes, the divergence error reduces with iterations. However, it will be shown by numerical tests that the divergence error reduces slowly as the meshes are made finer, a phenomenon which requires further investigation.

Although some investigators are against the idea of the eight-wave formulation, its success cannot be underestimated. It is expected that the recent increase in the development of such schemes (whether they use eight-wave formulation or not) for the solutions of MHD equations in all flow regimes will lead to more accurate investigation of the fusion plasma dynamics and play an important role in alternative energy production in the future.

In the next section, the idea of multidimensional FS schemes originally developed by Roe [10] will be described in detail. This section will include the description of the FS scheme for scalar advection. Then, how this scheme can be extended to the system of equations by means of a wave model will be discussed in detail. Section 3 will then describe the FS wave model, MHD-A, for the planar MHD equations. The numerical results obtained on structured and unstructured meshes for the scalar advection and planar MHD equations will be given in Section 4. Finally, the conclusion and a look at future work will follow in Section 5.

2. THE FLUCTUATION SPLITTING AND WAVE MODELS

In order to understand how a fluctuation splitting scheme can be employed for numerical solutions of a system of hyperbolic equations, it is important to get acquainted with the details of the scheme for scalar convection since the system is linearized and solved by means of simple waves advecting independently.

2.1. *Scalar Convection*

The fluctuation splitting scheme was first proposed by Roe [23] for the numerical solution of linear convection equation

$$u_t + \vec{\lambda} \cdot \vec{\nabla} u = 0, \tag{1}$$

where $\vec{\lambda} = (a, b)$ is a constant vector. In the work presented here, the source effects are also considered so that the right side of the above equation is replaced by the source (S). In

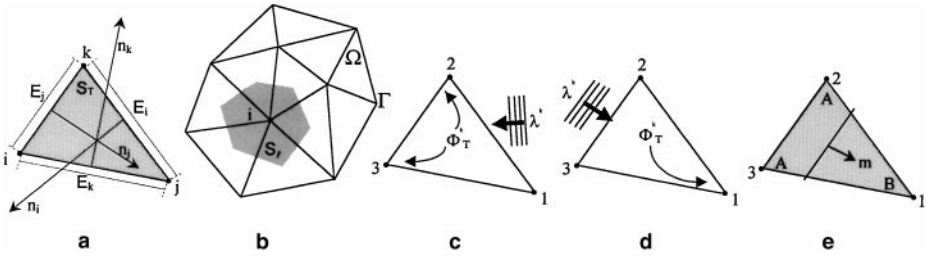

FIG. 1. (a) A triangular mesh with inward normals; (b) median dual cell area that weights node i; (c, d) upwind fluctuation distribution due to wave direction; (e) discontinuity capturing property of the scheme.

the FS scheme, the solution domain (Ω) including a total of N_T nodes is triangulated (see Fig. 1b), and the physical quantities stored at the vertices are approximated by a continuous piecewise linear function

$$u(\vec{x},t)=\sum_{i}^{N_T} N_i(\vec{x})u_i(t), \tag{2}$$

where, in finite element (FE) methods, N is called the nodal basis function which has the property $N_\ell(\vec{x}_k)=\delta_{k,l}$ where $\delta_{k,l}$ is the Kronecker delta function. Multiplying Eq. (1) by a weight function $w_\ell(\vec{x})$ and integrating over the solution domain (Ω) one gets the following equation for node ℓ:

$$\int\!\!\int_\Omega \left(w_\ell \frac{\partial}{\partial t}\sum_{k=1}^{N_T} N_k u_k\right) d\Omega + \int\!\!\int_\Omega \left(w_\ell \vec{\lambda}\cdot\sum_{k=1}^{N_T}\vec{\nabla}N_k u_k\right) d\Omega = \int\!\!\int_\Omega (w_\ell S)\, d\Omega. \tag{3}$$

Note that if the weight functions are identical to N_ℓ, the classical Galerkin FE method is obtained. Usually the global system (3) is built as a sum over the triangles, T,

$$\sum_T \left\{ \int\!\!\int_\Omega w_\ell \sum_{k=1}^{3} N_k \frac{\partial u_k}{\partial t}\, dS_T + \int\!\!\int_{S_T} w_\ell \lambda_i \sum_{k=1}^{3} \frac{\partial N_k}{\partial x_i} u_k\, dS_T = \int\!\!\int_\Omega w_\ell S\, dS_T \right\}, \tag{4}$$

where S_T is the area of triangle T and the sum inside every triangle runs from 1 to 3. For a linearly varying u on the triangle it can be verified that

$$\frac{\partial N_k}{\partial x_i}=\frac{n_{k,i}}{2S_T}, \qquad \frac{\partial u}{\partial x_i}=\frac{1}{2S_T}\sum_{k=1}^{3} n_{k,i}u_k, \tag{5}$$

where $n_{k,i}$ is the component of $\vec{n}_k$ in the x_i direction (i.e., inward normals shown in Fig. 1a). Using Eq. (5), the second integral in Eq. (4)—from now on called fluctuation, Φ_ℓ^T—simplifies to

$$\Phi_\ell^T = \sum_T \int\!\!\int_{S_T} w_\ell \lambda_i \sum_{k=1}^{3} \frac{n_{k,i}}{2S_T} u_k\, dS_T = \left(\frac{1}{S_T}\sum_T \int\!\!\int_{S_T} w_\ell\, dS_T\right)\Phi_T = \beta_\ell^T \Phi_T, \tag{6}$$

where β_ℓ^T are called distribution coefficents (satisfying $\beta_1^T+\beta_2^T+\beta_3^T=1$) since they distribute parts of the fluctuation (cell residual) to the three nodes of triangle T. The cell

fluctuation is then defined as

$$\Phi_T = \frac{1}{2}\sum_{p=1}^{3} \lambda_i n_{p,i} u_p = \sum_{p=1}^{3} k_p u_p, \tag{7}$$

since, from geometry, $\vec{n}_1 + \vec{n}_2 + \vec{n}_3 = 0$ (and hence $k_1 + k_2 + k_3 = 0$) and it can be shown that Φ_T can also be written as

$$\Phi_T = k_2(u_2 - u_1) + k_3(u_3 - u_1), \tag{8}$$

leading to a form which will be used later. The first integral in Eq. (4) leads to the product of $\partial u_k/\partial t$ and the so-called mass matrix M whose elements are defined as

$$M_{\ell,k} = \sum_T \int\int_{S_T} w_\ell N_k \, dS_T. \tag{9}$$

In the FE method it was found that taking $w_\ell = N_\ell$ (different from that in the spatial part) one gets the most stable Galerkin mass matrix for node k given by

$$M_{\ell,k} = \sum_T \int\int_{S_T} N_\ell N_k \, dS_T = \sum_{T\in\Omega_\ell} \frac{S_T}{3}\delta_{l,k} = S_\ell \delta_{l,k}, \tag{10}$$

where S_ℓ is now the area of the median dual cell of node ℓ (see Fig. 1b). The third integral Eq. (4) can be written as

$$\sum_T \int\int_{S_T} w_\ell S \, dS_T = \hat{S}_T, \tag{11}$$

where usually the source is split equally over the nodes of triangle T. Combining Eqs. (6), (9), (10) results in

$$S_\ell \frac{du_\ell}{dt} + \sum_T \beta_\ell^T \Phi_T = \hat{S}_T. \tag{12}$$

The Galerkin FE scheme is obtained by choosing $w_\ell = N_\ell$ in Eq. (3). In this case, the distribution coefficents turn into $\beta_\ell^{\mathrm{GAL}} = \frac{1}{3}$, leading to a method which is unstable for pure convection. For stability, an artificial dissipation term must be added, as is done in the Lax–Wendroff scheme, which leads to

$$\beta_\ell^{\mathrm{LW}} = \frac{1}{3} + \frac{\Delta t}{2S_T} k_\ell. \tag{13}$$

See [24] for different forms of the distribution function.

When a system of equations is considered, β_ℓ^T turn into matrices which should also satisfy $\sum_m \beta_m^T = I$ for consistency. In this case, the fluctation vector for system becomes

$$\Phi_T = \sum_{i=1}^{3} K_i U_i, \tag{14}$$

where U is the state vector and K_i are the jacobians based on edge normals, i.e.,

$$K_i = \frac{1}{2}(A_u n_{x,i} + B_u n_{y,i}) = \frac{1}{2} R_i \Lambda_i L_i, \tag{15}$$

where R, L, and Λ are associated eigenvector and eigenvalue matrices. In the FS scheme, either such matrices are directly used for distribution or the distribution is done by means of a consistent wave model. The second approach is considered is this paper.

The flow parameter, k_ℓ, distinguishes the inflow/outflow faces as well as the upstream/downstream nodes. For the system of equations, each wave of the associated eigensystem will have a different flow parameter and contribute to the total fluctuation in an upwind manner. When k_i is positive, the flow enters T through E_i, and i is the downstream node (while j and k are upstream nodes); otherwise, E_i is an outflow face and i is the upstream node. Note that because $\sum k_\ell = 0$, either one or two of k_ℓ must be negative. This fact leads to the development of different upwinding strategies using the sign of k_ℓ (i.e., see Figs. 1c and 1d for two- and one-node updates, respectively). For instance, defining a smart parameter $\sigma^* = |\sigma_1 + \sigma_2\sigma_3|/2$, where σ_ℓ is the sign of k_ℓ, one can distinguish one- and two-node updates. When $\sigma^* = 0$, it is a one-node update and the upwinding strategy requires that Φ_T should be assigned only to the upwind node, $i \equiv 2 + (\sigma_3 - \sigma_1)/2$ (i.e., $\beta_i = 1$, $\beta_j = \beta_k = 0$); otherwise, it is a two-node update case (i.e., $\sigma^* = 1$) and Φ_T is distributed between the nodes, $j \equiv 2 + (\sigma_3 - \sigma_2)/2$ and $k \equiv 2 + (\sigma_2 - \sigma_1)/2$ with different distribution weights β_j and β_k. Although, this procedure was developed by the author and it minimizes the number of "if" statements in coding, there exist different distribution schemes (see Paillere *et al.* [24] for a detailed review).

The discretized form of Eq. (12) leads to the following explicit local update, for each T which is not in equilibrium (i.e., has a finite fluctation):

$$u_\ell^{n+1} = u_\ell^n - \frac{\Delta t}{S_\ell} \sum_T \left[\beta_\ell^T \sum_{j=1}^{3} k_j u_j^n - \frac{1}{3} \hat{S}_T^n \right]; \tag{16}$$

here Δt is the time step and $n+1$ is the new time level. Notice that the average source is distributed equally to the nodes of T.

2.2. *Properties of FS Scheme*

The FS scheme is said to be locally *positive* (P) and hence nonoscillatory (i.e., the occurence of numerical oscillations which appears close to large changes in the solution is prohibited) when the new iterate u_ℓ^{n+1} is written as the convex average of old iterates as [21]

$$u_\ell^{n+1} = \sum_k C_k u_k^n, \tag{17}$$

with $C_k \geq 0$ for all k ($\sum C_k = 1$ for consistency). To show how this can be established in FS schemes, consider the one-node update and assume that node 1 is the downstream node. In this case, k_2, $k_3 \leq 0$ and $k_1 \geq 0$ by definition, and the total fluctuation is to be assigned to node 1 only (β_2, $\beta_3 = 0$ and $\beta_1 = 1$, see Fig. 1c). In this case, the updates for all three nodes

of T can be written as

$$S_1u_1 \leftarrow S_1u_1 - \Delta t\left[k_1u_1 + k_2u_2 + k_3u_3 - \frac{\hat{S}_T}{3}\right]; \qquad S_ju_j \leftarrow S_ju_j + \Delta t\frac{\hat{S}_T}{3}, \quad j = 2, 3 \tag{18}$$

so that positivity is achieved for $C_1 = S_1 - k_1\Delta t \geq 0$ or $\Delta t \leq S_1/k_1$, a condition that leads to the time step limitation. Note that, in the case of a system of equations, k_ℓ becomes the flow parameter of the ℓth eigenvalue, and $(u_2 - u_1)$ and $(u_3 - u_1)$ given in Eq. (8) turn into the gradients which are projected onto the associated eigenvector.

The FS scheme is said to be *linearity preserving* (LP) if the numerical scheme can reproduce steady linear solutions of Eq. (1) exactly. This property requires that, in the time evolution, $\Phi_T \to 0$ as the equilibrium is established in T so that no further update is sent to its nodes. Although, this is trivially satisfied for the one-node update, the design of LP schemes for the two-node updates leads to complications since β_ℓ^T should be designed as bounded. An N-scheme is a positive scheme with the lowest cross diffusion of its class and is closely related to the FE method developed by Hughes *et al.* [25]. In this scheme, for the two-node update case, the advection speed is written as the sum of components parallel to the edges of T across the downstream nodes (for instance, Fig. 1d shows that the downstream nodes are 2 and 3). The straightforward algebra shows that the fluctuations assigned to these nodes should be given by $\Phi_2 = k_2(u_2 - u_1)$ and $\Phi_3 = k_3(u_3 - u_1)$ (i.e., the parts of Eq. (8)) for upwinding and the condition $\Delta t \leq \min(S_2/k_2, S_3/k_3)$ should be satisfied for local positivity. In order to increase the spatial accuracy of this scheme to second order, the formulation presented by Sidilkover [26] can be used. In this formulation, recall that the N scheme leads to the two-node updates

$$S_1u_1 \leftarrow S_1u_1 + \Delta t\left[\frac{\hat{S}_T}{3}\right]; \qquad S_ju_j \leftarrow S_ju_j - \Delta t\left[k_j(u_j - u_1) - \frac{\hat{S}_T}{3}\right], \quad j = 2, 3 \tag{19}$$

and introduce a limiter function (Ψ) as a function of the ratio of two fluctuations, $Q = -\Phi_3/\Phi_2$. Then transfer the limited contribution $\Psi(Q)\Phi_2$ from u_2 to u_3 to increase the spatial accuracy of the scheme to second order without any requirement of the information from adjacent cells. This procedure is just adding an anti-diffusion term to the N scheme to make it LP. Thus the two-node updates in Eqs. (19) turn into

$$S_2u_2 \leftarrow S_2u_2 - \Delta t\left[\Phi_2 - \Psi\Phi_2 - \frac{\hat{S}_T}{3}\right], \qquad S_3u_3 \leftarrow S_3u_3 - \Delta t\left[\Phi_3 + \Psi\Phi_2 - \frac{\hat{S}_T}{3}\right], \tag{20}$$

which can also be written as

$$S_2u_2 \leftarrow S_2u_2 - \Delta t\left[\Phi_2(1-\Psi(Q)) - \frac{\hat{S}_T}{3}\right], \qquad S_3u_3 \leftarrow S_3u_3 - \Delta t\left[\Phi_3(1-\Psi(1/Q)) - \frac{\hat{S}_T}{3}\right], \tag{21}$$

where the coefficents of Φ_2 and Φ_3 are the nonlinear distribution functions $\beta_2 = 1 - \Psi(Q)$ and $\beta_3 = 1 - \Psi(1/Q)$, where, for boundness, the limiter should satisfy $0 \leq \Psi$, $\Psi(Q)/Q \leq 1$ for local positivity or $0 \leq \Psi \leq 2$ for global positivity. For instance, the minmod limiter $\Psi(r) = \max(0, \min(r, 1))$ and Superbee limiter $\Psi(r) = \max(0, \max(\min(2r, 1), \min(r, 2)))$ are examples of such limiters which satisfy local and global positivity, respectively. The

N scheme with limiters is called a nonlinear N scheme (or NN scheme) and the reader is referred to Refs. [24, 26, 28] for detailed reviews of different distribution schemes. On structured meshes, the spatial accuracy of the linear FS schemes is second order provided that the schemes include LP property. Even though the local truncation error for a single triangle may not seem to converge to zero as the mesh is refined, the global convergence and second order accuracy of the NN scheme (when all neighboring triangles are considered) have been proved by Perthame [27]. In the finite volume or finite difference schemes, the spatial second order accuracy requires information from neighboring cells. In contrast, it is remarkable that the FS schemes produce results as good as those obtained from such conventional schemes, although the operations are confined to only a single cell [28].

The FS scheme explained here can be extended to the nonlinear advection case in which the advection speed is approximated by some average and to the system of equations in which the fluctuation is treated as a sum of linearized simple wave fluctuations. For the scalar advection in 1D there is only one simple wave, moving forward or backward; however, in 2D, the orientation angle of the wave adds additional degree of freedoms. For the system of equations the complexity is further increased due to the existence of several waves and their possible propagation directions.

2.3. *System of Equations*

In this work, the conservative forms of MHD equations are integrated, although the primitive forms of the equations are utilized to derive an eigensystem suitable for the FS wave model MHD-A. A nonlinear system of 2D hyperbolic equations is given by the conservative form

$$\frac{\partial \mathbf{U}}{\partial t} + \frac{\partial \mathbf{F}}{\partial x} + \frac{\partial \mathbf{G}}{\partial y} = \mathbf{S} \tag{22}$$

or by the quasi-linear form

$$\frac{\partial \mathbf{U}}{\partial t} + (\hat{A}_u, \hat{B}_u) \cdot \vec{\nabla}\mathbf{U} = \mathbf{S}, \tag{23}$$

where the matrices $\hat{A}_u = \frac{\partial \mathbf{F}}{\partial \mathbf{U}}$ and $\hat{B}_u = \frac{\partial \mathbf{G}}{\partial \mathbf{U}}$ are conservative flux jacobians which give rise to a hyperbolic system provided that they have a real set of eigenvalues and a complete set of right and left eigenvectors. $\mathbf{U}$ is the conservative state vector (including density, momenta, magnetic field, and total energy, i.e., $\mathbf{U} = [\rho, \rho\mathbf{V}, \mathbf{B}, E]^T$, where $E = P/(\gamma - 1) + 1/2\rho V^2 + B^2/8\pi$, P is the pressure, and γ is the ratio of specific heats); $\mathbf{F}$, $\mathbf{G}$ are flux vectors, and $\mathbf{S}$ is the source vector (which may include the physical sources as well as the curvature terms and divergence source as will be explained later).

In order to solve Eq. (22) numerically, integrate it over triangle T with area Ω_T,

$$\int\int_T \mathbf{U}_t \, d\Omega = \Phi_T = -\int\int_T \left[\frac{\partial \mathbf{F}}{\partial x} + \frac{\partial \mathbf{G}}{\partial y} - \mathbf{S}\right] d\Omega, \tag{24}$$

or use Eq. (23) to obtain

$$\int\int_T \mathbf{U}_t \, d\Omega = \Phi_T = -\int\int_T [\hat{A}_u \mathbf{U}_x + \hat{B}_u \mathbf{U}_y - \mathbf{S}] \, d\Omega, \tag{25}$$

where $\mathbf{U}$ is assumed to be stored at the vertices as in scalar case. Assume further that $\mathbf{U}$ is approximated by Eq. (2) so that, since it varies linearly, its gradient is constant over T. If, in addition, $\hat{A}_u$ and $\hat{B}_u$ had been linear in $\mathbf{U}$, the above integration could have been performed exactly and Φ_T would have been equivalent to an explicit flux integral along the sides of T. Unfortunately, the conservative jacobians are not linear in the components of $\mathbf{U}$ for both the Euler and MHD equations, and the exact evaluation of Eq. (25) is not practical. Thus, the FS scheme requires that a decision be made on the numerical calculation of the jacobians since an incorrect calculation may lead to numerical waves propagating with wrong speed or directions. As suggested by Roe [28] this problem can be overcome by using a parameter state vector ($\mathbf{Z}$) such that $\mathbf{F}$, $\mathbf{G}$, and $\mathbf{U}$ are all quadratic, and the jacobians $A_z = \frac{\partial \mathbf{F}}{\partial \mathbf{Z}}$, $B_z = \frac{\partial \mathbf{G}}{\partial \mathbf{Z}}$, and $U_z = \frac{\partial \mathbf{U}}{\partial \mathbf{Z}}$ are all linear in the components of $\mathbf{Z}$. If, in addition, $\mathbf{Z}$ is assumed to vary linearly satisfying the same form as Eq. (2), the average $\bar{\mathbf{Z}}$ from which the elements of jacobians are obtained can easily be found from

$$\bar{\mathbf{Z}} = (\mathbf{Z}_i + \mathbf{Z}_j + \mathbf{Z}_k)/3, \tag{26}$$

where i, j, k are the vertices of the triangle.

By construction, the conservative property of the linearized system requires that the Rankine–Hugoniot (RH) conditions

$$\vec{\nabla} \cdot \vec{\mathbf{F}} = [A_u(\bar{Z}), B_u(\bar{Z})] \cdot \vec{\nabla}\mathbf{U} \qquad \text{with } \vec{\mathbf{F}} = (\mathbf{F}, \mathbf{G}) \tag{27}$$

are satisfied in both smooth and discontinuous parts of the flow. How this is satisfied by the FS scheme is explained by using Gauss's law in the homogeneous part of Eq. (24) to get

$$\Phi_T^H = -\int\int [\vec{\nabla} \cdot \vec{\mathbf{F}}]\, d\Omega = \oint_{\Gamma_T} (\mathbf{F}, \mathbf{G}) \cdot d\vec{n}, \tag{28}$$

where $d\vec{n}$ is directed inside the triangles. In this case, Φ_T^H can be written as

$$\begin{aligned} \Phi_T^H &= \int\int \frac{\partial \vec{F}}{\partial \mathbf{Z}} \frac{\partial \mathbf{Z}}{\partial \mathbf{U}} \cdot \vec{\nabla}\mathbf{U}\, d\Omega \\ &= \hat{A}_z \hat{\mathbf{U}}_z^{-1} \cdot \int\int \vec{\nabla}\mathbf{U}\, d\Omega = \frac{\partial \hat{\vec{F}}}{\partial \mathbf{U}} \cdot \oint \mathbf{U}\vec{n}\, d\ell = \hat{A}_z(\bar{Z}) \sum_{i=1}^{3} U_i \vec{n}_i. \end{aligned} \tag{29}$$

Now assume there exists a discontinuity in the solution and it propagates along a gradient direction, say $\vec{m}$, through a triangular mesh (as shown in Fig. 1e). In this case, the flux integration around this triangle becomes

$$\begin{aligned} \sum_{i=1}^{3} \vec{F}_i \cdot \vec{n}_i &= \vec{F}_1 \cdot \vec{n}_1 + \vec{F}_2 \cdot \vec{n}_2 + \vec{F}_3 \cdot \vec{n}_3 = \vec{F}_B \cdot \vec{n}_1 + \vec{F}_A \cdot (\vec{n}_2 + \vec{n}_3) \\ &= (\vec{F}_B - \vec{F}_A) \cdot \vec{n}_1 = (\vec{F}_B - \vec{F}_A) \cdot \vec{m}; \end{aligned} \tag{30}$$

similarly, one can also write $\sum U_i \vec{n}_i = (U_B - U_A)\vec{m}$, so that the fluctuation in Eq. (28) leads to the RH conditions along the discontinuity

$$(F_B - F_A) = \hat{A}_u(\bar{Z})(U_B - U_A). \tag{31}$$

This linearization procedure is not unique and the appropriate choice of the parameter vector should be based as much as possible on computational cost as well as on physical motivation. For example, it was shown by Roe [28] that the following parameter vector gives rise to desired linearity in A_z, B_z, and U_z (for the 2D Euler system)

$$\mathbf{Z} = [\sqrt{\rho}, \sqrt{\rho}u, \sqrt{\rho}v, \sqrt{\rho}H]^T, \tag{32}$$

where $H = (E + P)/\rho$ is the enthalpy. Using such a parameter vector, the fluctuation can be written as

$$\begin{aligned}\Phi_T &= \int\int \left[\mathbf{S} - \left(\frac{\partial F}{\partial \mathbf{Z}}\mathbf{Z}_x + \frac{\partial G}{\partial \mathbf{Z}}\mathbf{Z}_y\right) d\Omega = \int\int [\mathbf{S} - (A_z, B_z)\cdot \vec{\nabla}\mathbf{Z}]\, d\Omega \\ &= [\hat{\mathbf{S}} - (\hat{A}_z, \hat{B}_z)\cdot \hat{\vec{\nabla}}\mathbf{Z}]\Omega_T = \left[\hat{\mathbf{S}} - \left(\hat{A}_z\hat{\mathbf{U}}_z^{-1}, \hat{B}_z\hat{\mathbf{U}}_z^{-1}\right)\cdot \hat{\vec{\nabla}}\mathbf{U}\right]\Omega_T \\ &= [\hat{\mathbf{S}} - (\hat{A}_u(\bar{\mathbf{Z}}), \hat{B}_u(\bar{\mathbf{Z}}))\cdot \hat{\vec{\nabla}}\mathbf{U}]\Omega_T,\end{aligned} \tag{33}$$

where, for example,

$$\hat{A}_z = \frac{1}{\Omega_T}\int\int A_z(\mathbf{Z})\, d\Omega = \sum_{i=1}^{3} A_z(Z_i) = A_z(\bar{Z}) \qquad \text{and} \qquad \hat{\mathbf{S}} = \frac{1}{\Omega_t}\int\int S(\mathbf{Z})\, d\Omega \tag{34}$$

and $\hat{\nabla}\mathbf{Z}$ is calculated from the analogue of Eq. (5).

Using the explicit time discretization as in the scalar case, the conservative update of $\mathbf{U}$, located at vertex ℓ, becomes

$$\mathbf{U}_\ell^{n+1} = \mathbf{U}_\ell^n - \frac{\Delta t^n}{\Omega_\ell}\sum_T \left[\sum_k \beta_{\ell,k}^T \Phi_T^k - \frac{\hat{\mathbf{S}}_T(\bar{Z})}{3}\right]\Omega_T, \tag{35}$$

where Φ_T^k is the conservative fluctuation associated with kth linearized wave and $\beta_{\ell,k}^T$ is the distribution function, i.e., the fraction of the fluctuation sent to vertex ℓ by this wave.

In this work, the time evolution is computed with the second order Runge–Kutta method which was proved to be positive [31]. This scheme is given by

$$\begin{aligned}\mathbf{U}_\ell^* &= \mathbf{U}_\ell^n + \Delta t^n \mathrm{Res}\left[U_\ell^n\right] \\ \mathbf{U}_\ell^{n+1} &= \frac{1}{2}\mathbf{U}_\ell^n + \frac{1}{2}\left(\mathbf{U}_\ell^* + \Delta t^n\, \mathrm{Res}[\mathbf{U}_\ell^*]\right),\end{aligned} \tag{36}$$

where $\mathrm{Res}\,[\mathbf{U}_\ell^n] = -\sum_T \Phi_T^n/\Omega_\ell$ is called the residual. This scheme is conservative and it leads to overall second order accuracy provided that the local accuracy is at least of second order (which is the fact satisfied by NN scheme).

2.4. *FS Wave Models*

In the FS scheme, the total fluctuation is decomposed into scalar components (ϕ_T^k) and then distributed independently to the nodes of T in an upwind manner. This procedure is carried out by means of a wave model in which the waves arising from the normal jacobian (such as given in Eq. (15)) satisfy certain properties. The derivation of a wave model is easier when the state for the primitive form of MHD equations (i.e., $\mathbf{W} = [\rho, \mathbf{V}, \mathbf{B}, P]^T$) is used since the eigensystem of its flux jacobian is less complicated and the eigensystem of

the conservative form can easily be obtained by using the state jacobian $\hat{U}_w = \partial \mathbf{U}/\partial \mathbf{W}$ and its inverse. It must be noted again that it is the average parameter vector, $\bar{\mathbf{Z}}$, from which the components of jacobians are evaluated. The quasi-linear form of the system of equations in terms of so-called primitive variables can be obtained by premultiplying Eq. (23) by $\mathbf{U}_w^{-1}$,

$$\frac{\partial \mathbf{W}}{\partial t} + A_w \frac{\partial \mathbf{W}}{\partial x} + B_w \frac{\partial \mathbf{W}}{\partial y} = S_w, \tag{37}$$

where $S_w = \mathbf{U}_w^{-1} S$ and $A_w = \mathbf{U}_w^{-1} A_u \mathbf{U}_w$, $B_w = \mathbf{U}_w^{-1} B_u \mathbf{U}_w$. In this 2D case, the matrices A_w and B_w do not commute, and the characteristic lines for unsteady equations cannot be defined explicitly unless these matrices are linearized and the residual (or fluctuation) is expressed as a sum of simple wave solutions, as Roe suggested for Euler equations [23].

Regardless of the fact that the sources affect the solution, one must integrate the homogeneous part of the equations in conservative form. After the wave model is constructed, the conservative integration is easily established by converting the primitive form of equations into a conservative form by means of $\mathbf{U}_w^{-1}$ and $\mathbf{U}_w$ (i.e., $\mathbf{U}_w \mathbf{W}_t = \mathbf{U}_t$, $\mathbf{U}_w A_w \mathbf{U}_w^{-1} = A_u$). To show how this is done and how an FS-wave model is derived, the homogeneous part of Eq. (37) is first linearized as

$$\mathbf{W}_t + [\hat{A}_w(\bar{Z}), \hat{B}_w(\bar{Z})] \cdot \vec{\nabla} \mathbf{W} = 0 \tag{38}$$

and then the fluctuation for the primitive form, $\Phi_w = -(\hat{A}_w, \hat{B}_w) \cdot \vec{\nabla} \mathbf{W}$, is treated as the sum of linearized simple wave solutions. Since the solutions of hyperbolic equations display a wavelike character, let $\mathbf{W} = \mathbf{W}(\xi)$, where $\xi = \vec{x} \cdot \vec{n}_\theta - \lambda_\theta t$ defines the wave front propagating along $\vec{n}_\theta = (\cos\theta, \sin\theta)$ with a speed of λ_θ. In this case, the time rate of $\mathbf{W}$ and its gradient across the wave front will be given by $\mathbf{W}_t = -\lambda_\theta \frac{d\mathbf{W}}{d\xi}$ and $\frac{d\mathbf{W}}{d\xi}\vec{n}_\theta$, respectively. Plugging these into Eq. (38) will then lead to

$$[-\lambda_\theta + (\hat{A}_w, \hat{B}_w) \cdot \vec{n}_\theta]\, d\mathbf{W} = 0, \tag{39}$$

which shows that λ_θ is an eigenvalue and $d\mathbf{W}$ is the corresponding eigenvector of the matrix $A_n = (\hat{A}_w, \hat{B}_w) \cdot \vec{n}_\theta$. Therefore, as long as $d\mathbf{W} \neq 0$ across the wave front, its gradient $(\vec{\nabla}\mathbf{W})$ can be projected onto the right eigenvectors of $(A_w)_n$. In that case, the flux change across the discontinuity will be proportional to the change in the conservative state by means of the RH conditions. The resulting eigenvalue problem is then defined as

$$A_n R_w = \Lambda R_w, \tag{40}$$

where $A_n = \hat{A}_w \cos\theta + \hat{B}_w \sin\theta$ is the so-called 2D primitive jacobian matrix, $\Lambda = \mathrm{diag}(\lambda_1, \lambda_2, \ldots, \lambda_N)$ are its eigenvalues, and R_w is the column matrix of its right eigenvectors (of which the kth component leads to the conservative one through the relation $r_u^k = U_w r_w^k$). These results show that the gradient $\vec{\nabla}\mathbf{W}$ (which can be obtained from $\partial \mathbf{W}/\partial \mathbf{Z} \vec{\nabla} \mathbf{Z}$) can be written as a superposition of N discrete waves summed overall possible directions $(\theta = 0, \ldots, 2\pi)$,

$$\nabla W = \sum_{\theta=0}^{2\pi} \sum_{k=1}^{N} \alpha_k \mathbf{r}_w^k \vec{n}_{\theta_k} \qquad \text{or} \qquad (\mathbf{W}_x, \mathbf{W}_y) = \sum_{\theta=0}^{2\pi} \sum_{k=1}^{N} \alpha_k \mathbf{r}_w^k (\cos\theta^k, \sin\theta^k), \tag{41}$$

where α_k corresponds to the discrete *strength* of the wave and θ^k represents its direction, which is allowed to differ for each wave. One of the simplest models of the form given by Eq. (41) is obtained from the basic identity [30]

$$\nabla W \sin(\theta_2 - \theta_1) = -\big(\vec{s}_{\theta_2} \cdot \vec{\nabla} W\big)\vec{n}_{\theta_1} + \big(\vec{s}_{\theta_1} \cdot \vec{\nabla} W\big)\vec{n}_{\theta_2}, \tag{42}$$

where $\vec{s}_{\theta_i}$ satisfies $\vec{s}_{\theta_i} \cdot \vec{n}_{\theta_i} = 0$. Denoting ith left and right eigenvectors of a primitive system as r_{θ_i} and ℓ_{θ_i} (with $r^m_{\theta_i} \ell^n_{\theta_i} = \delta_{mn}$) one can obtain a wave model by projecting each term of the right-hand side of Eq. (42) onto r_{θ_1} and r_{θ_2}:

$$\nabla W = \sum_{k=1}^{N_1} \alpha_1^k \mathbf{r}^k_{w_1} \vec{n}_{\theta_1} + \sum_{k=1}^{N_2} \alpha_2^k \mathbf{r}^k_{w_2} \vec{n}_{\theta_2}, \qquad N_1 + N_2 = N \tag{43}$$

$$\alpha^k_{\theta_1} = -\frac{1}{\sin(\theta_2 - \theta_1)} \vec{s}_{\theta_2} \cdot \ell^k_{\theta_1} \vec{\nabla} W, \qquad \alpha^k_{\theta_2} = \frac{1}{\sin(\theta_2 - \theta_1)} \vec{s}_{\theta_1} \cdot \ell^k_{\theta_2} \vec{\nabla} W. \tag{44}$$

This decomposition can be interpreted as a mesh-independent directional splitting scheme. For example, when $\theta_1 = 0$ and $\theta_2 = \pi/2$ the discrete x and y derivatives are treated independently regardless of the underlying grid [32]. In model MHD-A, $\theta_1 = \theta$ and $\theta_2 = \theta + \pi/2$ were taken, as these were proved to have produced excellent results in several FS-wave models for Euler systems [26, 28, 32].

It is expected that the gradient $\vec{\nabla}\mathbf{W}$ may lead to inconsistencies whenever the spatial gradients are large. For instance, the spurious pressures may not be able to be balanced with the velocity gradients for shear flows in Euler systems [23]. In addition, the fact that the propagation angles are dependent on the gradients will lead to spurious oscillations (slowing the convergence) whenever the gradients are negligible. Of course, the stagnation points will always cause problems if no preconditioning or implicit time stepping techniques are utilized. Most of these issues have been investigated extensively for the Euler equations; however, the behaviour of the incompressible MHD equations and the flow behaviour near the stagnation points need further investigation. Some of these issues are currently being investigated by the author.

The decomposition of $\nabla\mathbf{W}$ can be transformed to $\nabla\mathbf{U}$ using $\nabla\mathbf{U} = \mathbf{U}_w \nabla\mathbf{W}$. In this case, the conservative state and flux gradients become

$$\vec{\nabla}\mathbf{U} = \sum_k \alpha_k \mathbf{r}^k_u \vec{n}^k_\theta, \qquad \vec{\nabla}\mathbf{F} = (\hat{A}_u)_n \vec{\nabla}\mathbf{U} = \sum_k (\lambda_k)_n \alpha_k \mathbf{r}^k_u, \tag{45}$$

where $\mathbf{r}^k_u$ is the kth right eigenvector of $(\hat{A}_u)_n$ obtained from r^k_w by $r^k_u = U_w r^k_w$. Utilizing these gradients in Eq. (33) then leads to the conservative fluctuation

$$\Phi_T = \left[\hat{\mathbf{S}}(\bar{Z}) - \sum_k (\lambda_k)_n \alpha_k \mathbf{r}^k_u\right] \Omega_T \tag{46}$$

so that Eq. (35) becomes

$$\mathbf{U}^{n+1}_\ell = \mathbf{U}^n_\ell - \frac{\Delta t^n}{\Omega_\ell} \sum_T \left[\sum_k \beta^T_{\ell,k} (\lambda_k)_n \alpha_k \mathbf{r}^k_u - \frac{\hat{\mathbf{S}}(\bar{Z})}{3}\right] \Omega_T, \tag{47}$$

where $\beta^T_{\ell,k}$ is the fraction of Φ_T in T (see Eq. (35)) sent to vertex ℓ by the wave moving in the direction $\vec{n}^k_\theta$.

3. MHD-A: THE FS WAVE MODEL FOR MHD EQUATIONS

The ideal MHD describes the macroscopic behaviour of the plasma interacting with external and internal fields and assumes that the conditions

$$\frac{\lambda}{L} \ll 1, \qquad \frac{\epsilon}{T\sigma} \ll 1, \qquad \frac{V}{c} \ll 1, \tag{48}$$

hold, where ρ, V, T, and L are, respectively, the characteristic density, speed, time, and length scales for the problem; c is the speed of light; and σ and ϵ are the conductivity and dielectric constant of the fluid. With these assumptions, the ideal MHD equations are given by the following conservative form with a divergence source [1, 9, 10],

$$\frac{\partial}{\partial t}\begin{bmatrix} \rho \\ \rho\vec{V} \\ \vec{B} \\ E \end{bmatrix} + \vec{\nabla}\cdot\begin{bmatrix} \rho\vec{V} \\ \rho\vec{V}\vec{V} + P^\star - \frac{\vec{B}\vec{B}}{4\pi} \\ \vec{V}\vec{B} - \vec{B}\vec{V} \\ (E + P^\star)\vec{V} - \frac{\vec{B}}{4\pi}(\vec{B}\cdot\vec{V}) \end{bmatrix} = -\begin{bmatrix} 0 \\ \frac{\mathbf{B}}{4\pi} \\ \mathbf{V} \\ \frac{\mathbf{B}\cdot\mathbf{V}}{4\pi} \end{bmatrix}\vec{\nabla}\cdot\mathbf{B}, \tag{49}$$

where $P^\star = P + B^2/8\pi$ is the total pressure. Note that the divergence source is not a consequence of the wave model developed here and its existence would not make a physical difference as $\nabla\cdot\mathbf{B}$ should be maintained as zero. It must be noted that in the test problems presented in this paper, it was observed that the divergence source had only minor effects on the solution. Thus, it was not considered during the numerical iterations. The stabilization due to the divergence condition was achieved only by using the magnetic monopole wave. The eigenvalues and eigenvectors associated with the flux jacobian of these eight conservation laws are well known (see Jeffrey and Tanuiti [33]), and they correspond to one entropy wave travelling with speed V_n; two Alfven waves travelling with speed $V_n \pm u_A$; and four magnetoacoustic waves travelling with speeds $V_n \pm u_s$ and $V_n \pm u_f$, where u_A, u_s, and u_f are Alfven, slow, and fast magnetoacoustic speeds, respectively,

$$u_T^2 = \frac{B_T^2}{4\pi\rho}, \qquad u_A^2 = \frac{B_n^2}{4\pi\rho},$$

$$u_{s/f} = \left[\frac{1}{2}\left[a^2 + u_A^2 + u_T^2 \mp \left[\left(a^2 + u_A^2 + u_T^2\right)^2 - 4a^2u_A^2\right]^{1/2}\right]\right]^{1/2}, \tag{50}$$

where $B_T^2 = B^2 - B_n^2$ is the tangential magnetic field. In dimensional splitting approach, V_n and B_n should be considered as x or y components of the velocity and magnetic field.

As stated earlier, several Riemann-type upwind schemes based on a seven-wave system (with zero divergence source) have been developed [6–8, 16]. In this work, yet another approach that was first introduced by Aslan [1], then succesfully used by Powell [14, 15] and Gombasi *et al.* [21], will be used. In this approach, Eq. (49) is first reduced to its primitive form by means of U_w and U_w^{-1} and then the eigensystem of its flux jacobian is obtained. By taking the divergence source into account, it can be shown that the flux jacobian includes the original seven waves mentioned above plus another (numerical monopole) wave moving with the magnetoacoustic waves. It will be shown later that the strength of this wave is just the divergence of a magnetic field and it creates dissipation only in the neighborhood of nonzero divergence arising from the discretization errors in the magnetic field.

It must be noted here that the magnetic monopole wave and divergence source cannot be separated and should be employed together in order for the conservative form to be consistent with the nonconservative form of MHD equations; although the effects of divergence source is negligible.

The origin of the magnetic monopole wave and its stabilization effects can be described as follows: consider a fluid particle moving on a magnetic field line with a velocity $\mathbf{v}$. In this case, the total change of its displacement $\partial\ell$ will be given by $D\partial\ell/Dt = (\partial\ell\cdot\nabla)\mathbf{v}$. When the equation of continuity and Faraday's law of ideal MHD equations (without divergence source) are combined one obtains $D(\mathbf{B}/\rho)/Dt = (\mathbf{B}/\rho\cdot\nabla)\mathbf{v} + \mathbf{v}/\rho\nabla\cdot\mathbf{B}$. Comparing the total changes of $\partial\ell$ and $\mathbf{B}/\rho$ one sees that, provided they are parallel initially, these vectors will remain parallel only if the second term on the right side of $D(\mathbf{B}/\rho)/Dt$ vanishes. Otherwise, the fluid particle may cut lines of magnetic force contradicting the ideal MHD limit (i.e., the condition $\sigma\to 0$). As a result, the magnetic flux around the particle is not conserved and a spurious magnetic monopole is created. This phenomenon justifies why Faraday's law should include a source term related to the divergence of magnetic field to eliminate numerical magnetic monopoles (see Jackson [20]).

In order to understand how the divergence source arises from the modification of the flux jacobian ($A_u = \partial F/\partial U$), one observes that the 1D system $U_t + F_x = U_t + A_u U_x = 0$ can be replaced by $U_t + \tilde{A}_u U_x = S_{\text{div}}$, where $S_{\text{div}} = (\tilde{A}_u - A_u)U_x$ is the divergence source (appearing on the right side of Eq. (49)). Note that this procedure does not modify the original seven-wave structure but introduces a numerical magnetic monopole wave to create extra dissipation to eliminate the noncommutativity of the numerical divergence and curl operators. With this modification, the primitive jacobian A_w with a seven-wave structure turns into $\tilde{A}_w$ with an eight-wave structure

$$A_w = \begin{bmatrix} V_x & \rho & 0 & 0 & 0 & 0 & 0 & 0 \\ 0 & V_x & 0 & 0 & -bx & by & bz & \frac{1}{\rho} \\ 0 & 0 & V_x & 0 & -by & -bx & 0 & 0 \\ 0 & 0 & 0 & V_x & -bz & 0 & -bx & 0 \\ 0 & 0 & 0 & 0 & 0 & 0 & 0 & 0 \\ 0 & B_y & -B_x & 0 & -V_y & V_x & 0 & 0 \\ 0 & B_z & 0 & -B_x & -V_z & 0 & V_x & 0 \\ 0 & \gamma P & 0 & 0 & VB & 0 & 0 & V_x \end{bmatrix},$$

$$\tilde{A}_w = \begin{bmatrix} V_x & \rho & 0 & 0 & 0 & 0 & 0 & 0 \\ 0 & V_x & 0 & 0 & 0 & by & bz & \frac{1}{\rho} \\ 0 & 0 & V_x & 0 & 0 & -bx & 0 & 0 \\ 0 & 0 & 0 & V_x & 0 & 0 & -bx & 0 \\ 0 & 0 & 0 & 0 & V_x & 0 & 0 & 0 \\ 0 & B_y & -B_x & 0 & 0 & V_x & 0 & 0 \\ 0 & B_z & 0 & -B_x & 0 & 0 & V_x & 0 \\ 0 & \gamma P & 0 & 0 & 0 & 0 & 0 & V_x \end{bmatrix} \tag{51}$$

(where $bx = B_x/4\pi\rho$, etc., and $VB = (\gamma-1)(\mathbf{V}\cdot\mathbf{B})/4\pi$) producing $S^w_{\text{div}} = (\tilde{A}_w - A_w)W_x$. It was shown by Powell [14] that the eight-wave system with the magnetic monopole wave has the desirable property of reverting to the seven-wave system in 1D since the strength

of the divergence wave vanishes in 1D (i.e., $B_x = \text{const.}$). It must be noted here that the modified jacobian $\tilde{A}_u$ is not the jacobian of any flux; therefore, this idea works better with fluctuation splitting schemes in which no fluxes but only the jacobians are utilized.

Although the magnetic monopole wave is not a real MHD wave and the existence of the divergence source leads to a slightly nonconservative form, their magnitudes are very small numerically. It is noted that although the scheme described here maintains $\nabla \cdot \mathbf{B} = 0$ to truncation errors, these errors increase to $O(1)$ at discontinuities. Utilizing the magnetic monopole wave and divergence source can mostly solve this problem but cannot totally eliminate it. This is due to the numerical resistivity created by the dissipation. An explanation of this was given by Falle *et al.* [34].

In the FS scheme described here, the primitive form of planar MHD equations (where $\partial/\partial z = 0$, B_z, $V_z = 0$) in cartesian coordinates is considered. As stated previously, the first step in deriving an FS-wave model is to obtain, analytically, the eigensystem of a two-dimensional jacobian matrix, $A_n = \tilde{A}_w \cos\theta + \tilde{B}_w \sin\theta$, and then to project the gradients, $\nabla \mathbf{W}$, onto its right eigenvectors. In the FS scheme, the modified matrix $\tilde{A}_w$, given on the right of Eq. (51), and its counterpart $\tilde{B}_w$ are used to get A_n,

$$A_n = \begin{bmatrix} V_n & \rho\cos\theta & \rho\sin\theta & 0 & 0 & 0 \\ 0 & V_n & 0 & -by\sin\theta & by\cos\theta & \cos\theta/\rho \\ 0 & 0 & V_n & bx\sin\theta & -bx\cos\theta & \sin\theta/\rho \\ 0 & -B_y\sin\theta & B_x\sin\theta & V_n & 0 & 0 \\ 0 & B_y\cos\theta & -B_x\cos\theta & 0 & V_n & 0 \\ 0 & \rho a^2\cos\theta & \rho a^2\sin\theta & 0 & 0 & V_n \end{bmatrix}, \tag{52}$$

where $V_n = V_x\cos\theta + V_y\sin\theta$ is the normal speed in the direction of $\mathbf{n}_\theta$ and $a = \sqrt{\gamma P/\rho}$ is the sound speed. Since this matrix defines the planar MHD case, its eigensystem does not include Alfven waves explicitly, although the fast and slow waves do exist and they include a contribution from the Alfven speed. The eigenvalues of A_n are then given by $V_n - u_f$, $V_n - u_s$, V_n, V_n, $V_n + u_s$, $V_n + u_f$, where the only difference from the original set is the magnetic monopole wave associated by the eigenvalue of V_n (see Eqs. (50)). The straightforward algebra carried out for A_n leads to the following column matrix of right eigenvectors and row matrix of left eigenvectors (normalized with $l_i r_j = \delta_{i,j}$),

$$R_w = \begin{bmatrix} 1 & 0 & \rho & \rho & \rho & \rho \\ 0 & 0 & -r_{2s} & r_{2s} & -r_{2f} & r_{2f} \\ 0 & 0 & r_{3s} & -r_{3s} & r_{3f} & -r_{3f} \\ 0 & \cos\theta & r_{4s}\sin\theta & r_{4s}\sin\theta & r_{4f}\sin\theta & r_{4f}\sin\theta \\ 0 & \sin\theta & -r_{4s}\cos\theta & -r_{4s}\cos\theta & -r_{4f}\cos\theta & -r_{4f}\cos\theta \\ 0 & 0 & \rho a^2 & \rho a^2 & \rho a^2 & \rho a^2 \end{bmatrix}, \tag{53}$$

$$L_w = \begin{bmatrix} 1 & 0 & 0 & 0 & 0 & -1/a^2 \\ 0 & 0 & 0 & \cos\theta & \sin\theta & 0 \\ 0 & -l_{3f} & -l_{2f} & X\sin\theta & -X\cos\theta & -l_{4f} \\ 0 & l_{3f} & l_{2f} & X\sin\theta & -X\cos\theta & -l_{4f} \\ 0 & l_{3s} & l_{2s} & -X\sin\theta & X\cos\theta & l_{4s} \\ 0 & -l_{3s} & -l_{2s} & -X\sin\theta & X\cos\theta & l_{4s} \end{bmatrix}, \tag{54}$$

where

$$r_{2s/f} = [B_y u_{s/f} - \sqrt{4\pi\rho}\, a u_{f/s}\, \mathrm{Sign}(B_n) \sin\theta]/B_T \tag{55}$$

$$r_{3s/f} = [B_x u_{s/f} - \sqrt{4\pi\rho}\, a u_{f/s}\, \mathrm{Sign}(B_n) \cos\theta]/B_T \tag{56}$$

$$r_{4s/f} = 4\pi\rho\left(u_{f/s}^2 - u_B^2\right)/B_T \tag{57}$$

$$l_{2s/f} = [\mathrm{Sign}(B_n B_y) u_y u_{s/f} - a u_{f/s} \sin\theta]/2a\left(u_f^2 - u_s^2\right) \tag{58}$$

$$l_{3s/f} = [\mathrm{Sign}(B_n B_x) u_x u_{s/f} - a u_{f/s} \cos\theta]/2a\left(u_f^2 - u_s^2\right) \tag{59}$$

$$l_{4s/f} = \alpha_{f/s}/2\rho a^2, \tag{60}$$

with

$$u_B = \frac{|B|}{\sqrt{4\pi\rho}}, \qquad u_{x,y} = \frac{|B_{x,y}|}{\sqrt{4\pi\rho}}, \qquad \alpha_{f/s} = \frac{u_{f/s}^2 - u_B^2}{u_f^2 - u_s^2}, \qquad X = \frac{B_T}{8\pi\rho\left(u_f^2 - u_s^2\right)}, \tag{61}$$

where $B_T = B_y \cos\theta - B_x \sin\theta$ is the tangential magnetic field. Note that the angle θ has not been specified yet and how it can be obtained as a function of field gradients will be presented later.

The MHD equations are nonstrictly hyperbolic since there are some points at which the wave ordering required in strictly hyperbolic systems is destroyed and two or more wave speeds may coincide. In the FS wave model MHD-A, the slow and entropy eigenvectors become degenerate in two limits: when $B_T = 0$ and when $B = 0$. The first limit is possible in several cases (i.e., when $\mathbf{n}_\theta$ is along the magnetic stream lines, when $B_x \approx B_y$ and $\theta \approx \pi/4$, and when $|B_y| \ll 1$ and $\theta \approx 0$ or when $|B_x| \ll 1$ and $\theta \approx \pi/2$). The second limit describes the Euler case (i.e., $B = 0$), and this eigensystem should reduce to that of the Euler system in this limit. This cannot happen automatically in perpendicular MHD since the Alfven waves do not exist and the slow waves cannot be combined with them to result in an Eulerian shear wave (see [17] to understand how this works out). Thus, in this limit a switching is required in coding of MHD-A. The singularities in Eqs. (55)–(57), for the case $B_T = 0$, can be removed by using the identities

$$u_s u_f = a u_A, \qquad u_T^2 a^2 = \left(u^2 - u_B^2\right)(u^2 - a^2), \tag{62}$$

where u can be u_s or u_f. Defining also the parameters

$$\beta_{x,y} = \frac{B_{x,y} + \epsilon}{B_T + \sqrt{2}\epsilon}, \qquad \beta_{\mathrm{sign}} = \frac{\mathrm{Sign}\, B_n + \epsilon}{B_T + \sqrt{2}\epsilon}, \qquad \alpha_{fT} = \frac{\alpha_f + \epsilon}{B_T + \sqrt{2}\epsilon}, \tag{63}$$

one can see that the nonsingular forms of $r_{2s/f}$, $r_{3s/f}$, and $r_{4s/f}$ can be defined as

$$r_{2s} = \beta_y u_s - \beta_{\mathrm{sign}} \sqrt{4\pi\rho}\, a u_f \sin\theta, \qquad r_{2f} = \left[a^2 \cos\theta + \beta_y\left(u_f^2 - a^2\right)\right]/u_f \tag{64}$$

$$r_{3s} = -\beta_x u_s + \beta_{\mathrm{sign}} \sqrt{4\pi\rho}\, a u_f \cos\theta, \qquad r_{3f} = \left[a^2 \sin\theta - \beta_x\left(u_f^2 - a^2\right)\right]/u_f \tag{65}$$

$$r_{4s} = -4\pi\rho\alpha_{fT}\left(u_f^2 - u_s^2\right), \qquad r_{4f} = \left[\left(u_f^2 - a^2\right)(\beta_x B_x + \beta_y B_y) + B_T a^2\right]/u_f^2, \tag{66}$$

where ϵ is an arbitrary small number.

Note that finding a parameter vector, $\mathbf{Z}$, such that the jacobians A_z, B_z, and U_z are all linear in its components is rather difficult for MHD; however, this does not mean that it is impossible. For instance, even though Brio and Wu [6] had concluded that Roe's averaging that satisfies RH conditions did not exist for MHD equations for an arbitrary γ, it was later shown by Aslan [11] that Roe's averaging indeed existed for any value of γ. Despite the fact that no such parameter vector exists for 2D MHD equations as of today, the results in [11] led to the idea that the following parameter vector can be used in FS-wave models for MHD,

$$\mathbf{Z} = \left[\sqrt{\rho}, \sqrt{\rho}V_x, \sqrt{\rho}V_y, \frac{B_x}{\sqrt{\rho}}, \frac{B_y}{\sqrt{\rho}}, \sqrt{\rho}H^*\right]^T, \tag{67}$$

where $H^* = [E + P^*]/\rho$ is the total enthalpy. With this choice, most of the terms in the jacobians A_z, B_z become linear in the components of $\mathbf{Z}$ except that the terms related to the momentum and hence energy fluxes include some second order terms which usually introduce negligible errors. It was found by numerical experiments that a careful design of such a parameter vector is important for better resolution of the discontinuities for FS methods, although the parameter vector given by Eq. (67) produces rather impressive results for the model MHD-A, as will be shown in the next section.

As was shown in Section 2.4, the solution to the system of equations can be interpreted as the superposition of a discrete number of simple waves of which strengths and directions have not been specified yet. As discussed earlier, this so-called pattern recognition step is carried out by the projection of a two-dimensional state gradient onto the eigenvectors so that the correct discontinuity capturing property will have been embedded in the scheme. In 1D, consistent analysis of local gradient with the superposition of simple waves shows that one needs 7 wave strengths to match with 7 field gradients in MHD (note that $B_x = \text{const.}$ in 1D). Although the eigensystem of the flux jacobian indicates the existence of an entropy and magnetic monopole waves and four magnetoacoustic waves propagating (possibly) at different angles, model MHD-A includes four additional magnetoacoustic waves but only two angles, resulting in 12 parameters. Note that the space gradient has 6 components in x and 6 components in y direction, giving 12 equations. Thus the number of gradients can easily be matched with the 10-wave structure. As was stated by Roe [23], who developed Model-A for Euler equations, it was possible to consider more waves and fix some relations between them to balance with the right number of free parameters. The reason behind the choice of a set is its capability to resolve complex flow patterns such as intersecting shocks and contacts. One should always remember that wave models based on a rather limited number of waves may have problems resolving these flows, while a large number of waves may do better but each of them brings its own dissipation into the scheme. Additionally, when more waves than necessary are used, the balance among these waves will be the only mechanism which can drive the residual to zero as steady state is approached (instead of having velocities and strengths vanish [24]). Finally, the equations to solve for the angles and strengths become too complicated unless additional waves are utilized.

In the FS wave model presented here, both slow and fast magnetoacoustic parts of the total fluctuation are represented by four plane waves travelling orthogonally to one another. These include the fast waves labeled 5, 6, 9, 10 and the slow waves labeled 3, 4, 7, 8 in Fig. 2. The eight strengths (four slow and four fast) and an independent direction, θ, contribute nine parameters to the model. When the monopole wave strength, the entropy wave strength, and its direction ($\mathbf{n}_{\theta_e}$) are introduced as three more parameters, one can match the number of unknowns with the number of local gradients. As discussed earlier (see Eqs. (42, 43)), the

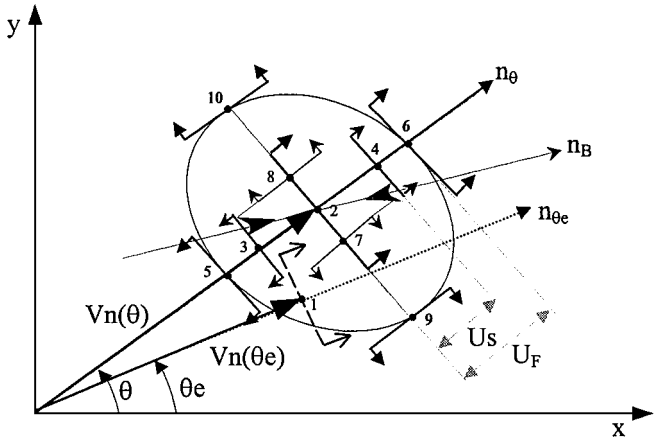

FIG. 2. The locations and directions of possible wave fronts existing in FS-wave model MHD-A for the case $|V_n| < u_f$. The waves labeled 1, 2 are entropy and numerical magnetic monopole waves; and those labeled 5, 6, 9, 10 are fast waves, and those labeled 3, 4, 7, 8 are slow waves.

existence of orthogonal magnetoacoustic waves moving with $\theta + \pi/2$ has useful properties such as introducing additional dissipation and representing the magnetoacoustic part of the flow by a couple of four plane wave sets, each representing one circular wave. It also seems that the assumption of orthogonality of the magnetoacoustic waves is crucial in producing equations for which a unique solution is possible.

In order to understand the 10-wave structure utilized in model MHD-A, see Fig. 2 for the positions and the directions of possible wave fronts after a time Δt (where all wave fronts were considered to have been located at the origin at $t = 0$). When all the contributions from these waves are considered, the gradient of W is written as

$$\vec{\nabla} W = \alpha_e^1 r_e^1 \vec{n}_{\theta_e} + \alpha_{\text{div}}^2 r_{\text{div}}^2 \vec{n}_\theta + \sum_{k=3}^{6} \alpha_\theta^k r_\theta^k \vec{n}_\theta + \sum_{k=7}^{10} \alpha_{\theta+\pi/2}^k r_{\theta+\pi/2}^k \vec{n}_{\theta+\pi/2}, \tag{68}$$

from which the unknown strengths can be found as follows by means of Eq. (43),

$$\alpha_e^1 = \vec{n}_e \cdot \left(l_{\theta_e}^1 \cdot \vec{\nabla} W\right), \qquad \alpha_{\text{div}}^2 = \vec{n}_\theta \cdot \left(l_\theta^2 \cdot \vec{\nabla} W\right) \tag{69}$$

$$\alpha_\theta^k = \vec{n}_\theta \cdot \left(l_\theta^k \vec{\nabla} W\right), k = 3, \ldots, 6, \qquad \alpha_{\theta+\pi/2}^k = \vec{n}_{\theta+\pi/2} \cdot \left(l_{\theta+\pi/2}^k \vec{\nabla} W\right), \quad k = 7, \ldots, 10, \tag{70}$$

provided that the propagation angles (θ and θ_e) are known. Note that this form is allowed due to Eq. (42) since the angles $\vec{n}_{\theta_1} = \vec{n}_\theta$ and $\vec{n}_{\theta_2} = \vec{n}_\theta + \pi/2$ satisfy the relation $\vec{n}_{\theta_1} \cdot \vec{n}_{\theta_2} = 0$. In this case, the gradients in the direction of $\vec{n}_\theta$ and those in perpendicular directions will be treated independently.

The propagation angle and the strength of entropy wave can easily be found by multiplying the first row of (54) by $\vec{\nabla} W$ and projecting it onto $\vec{n}_{\theta_e}$ (see Eq. (69)). This results in

$$\alpha_e = (\cos\theta_e, \sin\theta_e)[(1, 0, 0, 0, 0, -1/a^2) \begin{bmatrix} \rho_x & \rho_y \\ (V_x)_x & (V_x)_y \\ (V_y)_x & (V_y)_y \\ (B_x)_x & (B_x)_y \\ (B_y)_x & (B_y)_y \\ P_x & P_y \end{bmatrix}], \tag{71}$$

which turns into $\alpha_e = \cos\theta_e(\rho_x - P_x/a^2) + \sin\theta_e(\rho_y - P_y/a^2)$, giving

$$\tan\theta_e = \frac{\left(\rho_y - P_y/a^2\right)}{\left(\rho_x - P_x/a^2\right)}, \qquad \alpha_e = \sqrt{\left(\rho_x - P_x/a^2\right)^2 + \left(\rho_y - P_y/a^2\right)^2}. \tag{72}$$

Note that, not surprisingly, this is the same result that is obtained by any FS-wave model for the Euler equations. How the magnetic monopole wave strength and the angle θ are obtained can easily be seen by writing Eqs. (68) explicitly for the magnetic field gradients

$$\begin{aligned}\frac{\partial B_x}{\partial x} &= \alpha_{\text{div}}\cos^2\theta + [r_{4s}(\alpha_s^- + \alpha_s^+) + r_{4f}(\alpha_f^- + \alpha_f^+)]\sin\theta\cos\theta \\ &\quad - \left[r'_{4s}\left(\alpha_{s_{90}}^- + \alpha_{s_{90}}^+\right) + r'_{4f}\left(\alpha_{f_{90}}^- + \alpha_{f_{90}}^+\right)\right]\sin\theta\cos\theta \end{aligned} \tag{73}$$

$$\begin{aligned}\frac{\partial B_x}{\partial y} &= \alpha_{\text{div}}\sin\theta\cos\theta + [r_{4s}(\alpha_s^- + \alpha_s^+) + r_{4f}(\alpha_f^- + \alpha_f^+)]\sin^2\theta \\ &\quad + \left[r'_{4s}\left(\alpha_{s_{90}}^- + \alpha_{s_{90}}^+\right) + r'_{4f}\left(\alpha_{f_{90}}^- + \alpha_{f_{90}}^+\right)\right]\cos^2\theta \end{aligned} \tag{74}$$

$$\begin{aligned}\frac{\partial B_y}{\partial x} &= \alpha_{\text{div}}\sin\theta\cos\theta - [r_{4s}(\alpha_s^- + \alpha_s^+) + r_{4f}(\alpha_f^- + \alpha_f^+)]\cos^2\theta \\ &\quad - \left[r'_{4s}\left(\alpha_{s_{90}}^- + \alpha_{s_{90}}^+\right) + r'_{4f}\left(\alpha_{f_{90}}^- + \alpha_{f_{90}}^+\right)\right]\sin^2\theta \end{aligned} \tag{75}$$

$$\begin{aligned}\frac{\partial B_y}{\partial y} &= \alpha_{\text{div}}\sin^2\theta - [r_{4s}(\alpha_s^- + \alpha_s^+) + r_{4f}(\alpha_f^- + \alpha_f^+)]\sin\theta\cos\theta \\ &\quad + \left[r'_{4s}\left(\alpha_{s_{90}}^- + \alpha_{s_{90}}^+\right) + r'_{4f}\left(\alpha_{f_{90}}^- + \alpha_{f_{90}}^+\right)\right]\sin\theta\cos\theta, \end{aligned} \tag{76}$$

where the subscript 90 denotes the orthogonal waves and $r'_{4s,\,f}$ can be obtained from Eqs. (66) by replacing θ with $\theta + \pi/2$. From Eqs. (73) and (76) one immediately has

$$\alpha_{\text{div}} = \left(\frac{\partial B_x}{\partial x} + \frac{\partial B_y}{\partial y}\right) = \vec{\nabla}\cdot\mathbf{B}, \tag{77}$$

which shows that the strength of the numerical magnetic monopole wave equals the divergence of the magnetic field as anticipated earlier. Obviously, this wave has no action when the divergence condition is exactly satisfied. The effect of this wave becomes significant only in the regions where spurious magnetic monopoles are created due to the discretization errors in the divergence condition (i.e., near discontinuities). In this case, the dissipation introduced by magnetic monopole wave alters the evolution of magnetic field in such a way that the discretization errors are reduced significantly and the divergence condition is satisfied to within the accuracy of the scheme. This observation happens to be supported by numerical results that will be presented in the next section.

Using the trigonometric identities, Eqs. (73)–(76) lead to the relations

$$\begin{aligned}[(B_x)_x - (B_y)_y]\cos 2\theta &= \alpha_{\text{div}}\cos^2 2\theta + \left[r_{4s}(\alpha_s^- + \alpha_s^+) + r_{4f}(\alpha_f^- + \alpha_f^+)\right. \\ &\quad \left. - r'_{4s}\left(\alpha_{s_{90}}^- + \alpha_{s_{90}}^+\right) - r'_{4f}\left(\alpha_{f_{90}}^- + \alpha_{f_{90}}^+\right)\right]\sin 2\theta\cos 2\theta \end{aligned} \tag{78}$$

$$\begin{aligned}[(B_x)_y + (B_y)_x]\sin 2\theta &= \alpha_{\text{div}}\sin^2 2\theta - \left[r_{4s}(\alpha_s^- + \alpha_s^+) + r_{4f}(\alpha_f^- + \alpha_f^+)\right. \\ &\quad \left. - r'_{4s}\left(\alpha_{s_{90}}^- + \alpha_{s_{90}}^+\right) - r'_{4f}\left(\alpha_{f_{90}}^- + \alpha_{f_{90}}^+\right)\right]\sin 2\theta\cos 2\theta, \end{aligned} \tag{79}$$

from which one obtains

$$[(B_x)_x - (B_y)_y]\cos 2\theta + [(B_x)_y + (B_y)_x]\sin 2\theta = \alpha_{\text{div}}, \tag{80}$$

resulting in

$$\tan 2\theta = \frac{(B_x)_y + (B_y)_x}{(B_x)_x - (B_y)_y}. \tag{81}$$

This result is independent of the existence of magnetic monopole wave and is rather interesting and physically meaningful since it can be derived from another perspective as well. If the magnetic field (including gradients) at two infinitesimally near locations, $\mathbf{r_0}$ and $\mathbf{r} = \mathbf{r_0} + \delta\mathbf{r}$ (where $\mathbf{r_0} = (\epsilon\cos\psi, \epsilon\sin\psi)$), are considered, one has

$$\mathbf{B}(\mathbf{r}) = \mathbf{B}_0(\mathbf{r_0}) + \frac{\partial\mathbf{B}}{\partial x}\delta\mathbf{x} + \frac{\partial\mathbf{B}}{\partial y}\delta\mathbf{y} + \mathrm{O}(2), \tag{82}$$

where $\mathbf{B}_0 = (B_0\cos\psi,\, B_0\sin\psi)$ and $\delta\mathbf{r} = (\delta\mathbf{x},\, \delta\mathbf{y}) = \delta\epsilon(\cos\psi,\, \sin\psi)$. In this case, the magnetic field can be written as

$$\mathbf{B} = [(B_0 + (B_x)_x\delta\epsilon)\cos\psi + (B_x)_y\delta\epsilon\sin\psi,\, (B_0 + (B_y)_y\delta\epsilon)\sin\psi + (B_y)_x\delta\epsilon\cos\psi] \tag{83}$$

or

$$B^2 = B_0^2 + 2B_0\big[(B_x)_x\cos^2\psi + (B_y)_y\sin^2\psi + ((B_x)_y + (B_y)_x)\sin\psi\cos\psi\big]\delta\epsilon \tag{84}$$

up to first order in $\delta\epsilon$. Notice that the gradient in the magnetic field has caused deformation in the original configuration. The principal axis of this deformed ellipse (shown in Fig. 2) is represented by $\frac{dB}{d\psi} = 0$, resulting in

$$[(B_y)_y - (B_x)_x]\sin 2\psi + [(B_x)_y + (B_y)_x]\cos 2\psi = 0, \tag{85}$$

which leads to $\tan 2\psi = ((B_x)_y + (B_y)_x)/((B_x)_x - (B_y)_y)$, the same result as Eq. (84). Note that this angle also cancels the second term on the right-hand side of Eq. (84), resulting in the conservation of the magnitude of the magnetic field. This result shows that the magnetoacoustic waves produced by the FS-wave model MHD-A are aligned with the directions of maximum and minimum magnetic-strain rates in the magnetofluid. This observation also justifies why orthogonal magnetoacoustic waves are considered in the wave model.

The strengths of the slow and fast magnetoacoustic waves can be found from Eq. (70) and are given, respectively, by

$$\alpha_\theta^{3/4} = \mp l_{3f}^\theta\left(\cos\theta\frac{\partial V_x}{\partial x} + \sin\theta\frac{\partial V_x}{\partial y}\right) \mp l_{2f}^\theta\left(\cos\theta\frac{\partial V_y}{\partial x} + \sin\theta\frac{\partial V_y}{\partial y}\right) \tag{86}$$

$$\alpha_\theta^{5/6} = \pm l_{3s}^\theta\left(\cos\theta\frac{\partial V_x}{\partial x} + \sin\theta\frac{\partial V_x}{\partial y}\right) \mp l_{2s}^\theta\left(\cos\theta\frac{\partial V_y}{\partial x} + \sin\theta\frac{\partial V_y}{\partial y}\right) - \frac{X}{2}\left(\frac{\partial B_x}{\partial y} - \frac{\partial B_y}{\partial x}\right) + l_{4s}^\theta\vec{\nabla}P, \tag{87}$$

where $\vec{\nabla}P = \cos\theta\, P_x + \sin\theta\, P_y$ is the pressure gradient. Replacing the angle θ with $\theta + \pi/2$ in Eq. (86) and (87) leads to the remaining strengths $\alpha_{\theta+\pi/2}^{7/8}$ and $\alpha_{\theta+90}^{9/10}$.

Having the propagation angle of magnetoacoustic waves dependent only upon the magnetic field gradients is interesting. However, one should attempt to find the dependence of these angles on the velocity gradients as well in order to be able to specify a nonsingular limit of $B \to 0$. This requires the solution of nonlinear relations between the magnetic field and velocity gradients. Even though this procedure is very complicated, without this, the models such as MHD-A will perform poorly especially for the high beta flows, where the magnetic field pressure ($B^2/8\pi$) is negligible in comparison with the scalar pressure, P. This issue and the performance of the code at subsonic flows and at stagnation points are currently being investigated by the author and will be the subject of subsequent papers.

With the results presented in this section, the derivation of FS-wave model MHD-A is thus completed. In summary, the 2D algorithm is implemented as follows. At time t^{n+1}, where Δt is calculated from CFL $\min(dx, dy)/[\max(|\mathbf{V}|)^n + \max(u_f)^n]$ for each T with local nodes $\ell = 1, 2, 3$,

—get $\bar{\mathbf{Z}}$ and $\vec{\nabla}\mathbf{Z}$ from Eqs. (5) and (26) and obtain $\vec{\nabla}\mathbf{W}$ using $\partial\mathbf{W}/\partial\mathbf{Z}$ to be used to evaluate the angles θ_e and θ from Eqs. (72) and (81);

—then for each k evaluate the wave strengths using Eqs. (72), (77), (86), and (87) and the wave speeds(λ_k) and right eigenvectors (r_u^k) using Eqs. (50) and (53), respectively;

—then use Eq. (47) to update the nodes by upwinding with a procedure explained in Eq. (20) depending on each flow parameter ($k_k = \lambda_x^k \cos\theta + \lambda_y^k \sin\theta$) and on distribution coefficents, $\beta_{\ell,k}^T$.

—After the procedure is repeated for each k and T, the predictor part of Eq. (36) will have been completed and $\mathbf{U}_\ell^*$ will have been obtained;

—finally repeat all the above procedure to obtain the state at new time step, $\mathbf{U}_\ell^{n+1}$ from the corrector part of Eq. (36).

4. NUMERICAL RESULTS

4.1. *Scalar Advection*

The first test presented is the scalar nonlinear advection governed by Burger's equation. This test case was chosen to show the resolution property of the FS scheme for a shock formation due to converging characteristics. In this problem, $\vec{\lambda} = (u, 1)$ was used (i.e., the nonlinear problem $u_t + uu_x + u_y = 0$ was solved), and the boundary values of u on the left, right, and lower boundaries were taken as $u = 1.5$, $u = -0.5$, and $u = 1.5 - 2x$, respectively. The problem was initialized with $u = 0$ and solved by the scheme described in Section 2.1 on a 30×30 square domain ($x, y : [0, 1]$) covered by triangles with right-running diagonals. The numerical result obtained after the residual reduced to machine zero is depicted in Fig. 3a. It is seen that the scalar FS scheme described in Section 2.1 (with Superbee limiter) is capable of solving steady state nonlinear problems rather accurately, capturing the shock over two or three cells without spreading.

The next test problem is the circular advection with nonuniform velocity: $\vec{\lambda} = (y, -x)$. In this test problem, the left half of the lower boundary is kept at $u = 0$ if $x < -0.65$, $u = 1$ if $-0.65 < x < -0.35$, and $u = 0$ if $-0.35 < x < 0$ and the left and upper boundaries are kept at $u = 0$. This problem was initialized as before and solved on the same grid (but in this case with $x : [-1 : 1]$). The exact solution for this test problem is a discontinuous advection (with $u = 1$ between two half circles). As seen from Fig. 3b, this is represented very well by the numerical solution, and the discontinuity shows only a small amount of

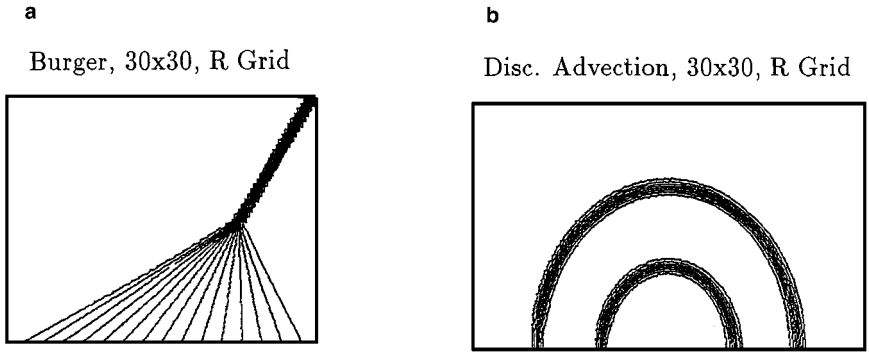

FIG. 3. The contours of u obtained by scalar advection test cases (obtained on 30×30 coarse grid): (a) nonlinear Burger's problem; (b) circular discontinuous advection problem.

spreading during the transient stage. This shows that the distribution algorithm described in Section 2.1 produces better results than those presented in [24].

4.2. *Zachary's Sonic Test Problem with* $B_x = 0$

In order to check the performance of the model MHD-A in 1D limit, the strong sonic problem introduced by Zachary *et al.* [7] was solved on a highly elongated isotropic triangular grids of different resolutions. As an initial condition, the x axis is divided into two halves and the following states are defined on both sides (with $\gamma = 5/3$):

$$\mathbf{W}^{\mathrm{L}} = [1, 0, 0, 0, \sqrt{4\pi}, 1000], \qquad \mathbf{W}^{\mathrm{R}} = [0.125, 0, 0, 0, -\sqrt{4\pi}, 0.1].$$

With this choice of initial conditions, the strong pressure gradient and the initial discontinuity in the tangential magnetic field gives ris to a left moving rarefaction wave and a right moving contact discontinuity behind a fast shock. Since $B_x = 0$ and practically the 1D problem is solved on a 2D mesh, the time evolutions of ρ and B_y have the same form (i.e., $\rho_t + (V_x\rho)_x = 0$ and $(B_y)_t + (V_x B_y)_x = 0$). Thus across shocks and rarefactions, B_y/ρ should be constant. By using the numerical scheme summarized at the end of Section 3, this problem was solved on isotropic grids with four different resolutions (100×20, 200×20, 400×20, 800×20), and resulting density and B_y profiles at $t = 0.003$ are depicted in Fig. 4 along with the analytical solution as straight line. Although the contact discontinuity

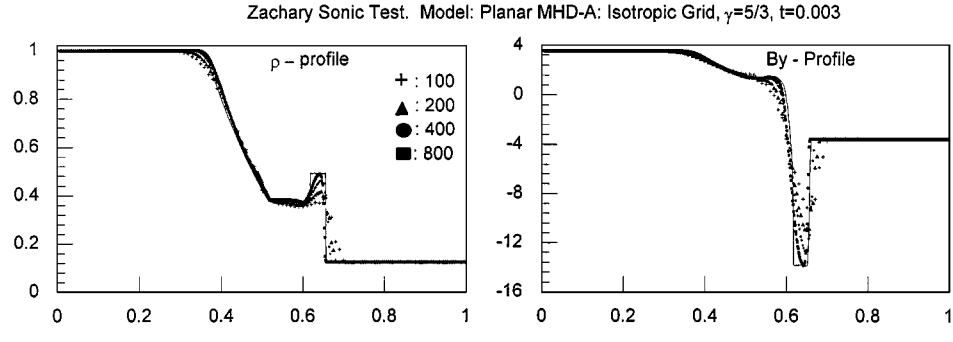

FIG. 4. The density, B_y, profiles obtained on 100×20, 200×20, 400×20, and 800×20 grids at $t = 0.003$. The plots show the 1D feature of the solution along the center line $y = 0.5$ for Zachary's sonic test problem. The continuous line shows the analytical solution.

is slightly smeared, it is seen that the solutions converge to the correct jump conditions (the jumps in ρ and B_y are about 3.9 across the shock) as the grid resolution is increased. Note that since the problem is practically 1D (i.e., $B_x = 0$ and $\partial B_y/\partial y = 0$), the magnetic monopole wave and divergence source have no effect on the solutions.

4.4. *Author's Contact Discontinuity Test*

The next test problem is the MHD version of classical Mach = 2.9 flow in a rectangular domain of $[0, 4] \times [0, 1]$ introduced by Aslan [13] and it is an excellent test case to show the ability of magnetic monopole wave to get physically correct solutions, i.e., a 29° supersonic shock reflecting from the lower boundary. The states to be used on the left and upper boundaries are (with $\gamma = 1.4$)

$$\mathbf{W}^{\mathrm{L}} = [1, 2.9, 0, \sqrt{\pi}, 0, 1/\gamma], \qquad \mathbf{W}^{\mathrm{U}} = [1.46, 2.717, -0.405, 2.424, -0.361, 1.223],$$

such that the RH conditions are satisfied across the shock as found in [13]. Note that the only action performed on the lower boundary was to set V_y to zero to accomplish reflection and the states on the right boundary were simply untouched during iterations to make this boundary outgoing. The problem was solved numerically on 120×60 isotropic grid, and the steady state gray scale images of B_y obtained without and with magnetic monopole wave (the divergence source was not used) are shown in Fig. 5. As seen, without the magnetic monopole wave (Fig. 5a) the magnetic field displays magnetic wells and spurious oscillations in the region between the shocks and an unphysical discontinuity across the reflected shock towards the right boundary. In contrast, the solution with the magnetic monopole wave and divergence source (Fig. 5b) is excellent since the shock locations are correct, shocks remain uniform and sharp before and after reflection, and no problems exist at the outgoing boundary. These results show that the divergence source has only a minor effect in eliminating problems due to divergence constraints and it is mainly the magnetic monopole wave which stabilizes the scheme. It is noted that this is not the case for the finite volume-type schemes, which require both the divergence source and magnetic monopole wave for stabilization unless other stabilization methods are not utilized. Thus the method derived here differs from those that were presented in [9, 13, 14].

4.5. *Author's Blast Wave Test*

We now examine the blast wave test (introduced by Aslan [13]) in free space influenced by arbitrarily directed magnetic field. The blast wave is driven by high pressure and high temperature in a circular region of radius 0.2 within a square region ($x : [-1 : 0]$, $y : [0 : 1]$). The

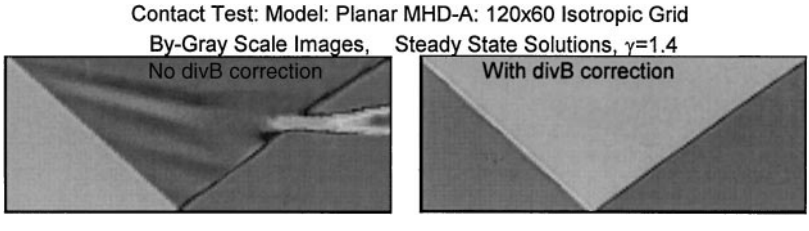

FIG. 5. The gray scale images of B_y obtained by the scheme described by Eq. (36) with and without magnetic monopole wave.

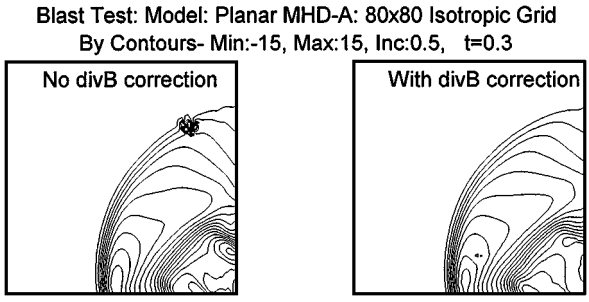

FIG. 6. The contours of B_y obtained by the scheme described at the end of Section 3 for the blast wave test without and with magnetic monopole wave and divergence source.

initial conditions are (with $\gamma = 1.4$) $\mathbf{V} = 0$, $B_x = 3$, $B_y = 1$ and $P^{\text{in}} = 50$, $\rho^{\text{in}} = 20$, $P^{\text{out}} = 1$, $\rho^{\text{out}} = 1$. Figure 6 shows the resulting B_y contours, obtained on an 80×80 isotropic grid with the scheme described at the end of Section 3, with and without the magnetic monopole wave at $t = 0.3$. Again, the solution without the magnetic monopole wave (Fig. 6a) shows nonphysical magnetic islands (due to a numerical magnetic monopole created by numerics) near the upper left part of the expanding shock, correcting the comments given by Falle *et al.* [34]. After a careful examination of physical variables near singular point, it was found that the entropy and circulation grow exponentially during iterations, leading to the nonphysical dynamics near this point. In most cases, this situation causes the codes to crash when this phenomenon reaches intolerable levels. The solution with the magnetic monopole wave (Fig. 6b) includes no such problems, thus showing the ability of the magnetic monopole wave to eliminate nonphysical magnetic monopoles and hence nonphysical dynamics. The results show that after the explosion, a rarefaction wave moves inwards and a contact discontinuity behind a strong shock move outwards. In addition, the existence of oblique magnetic field disturbs the symmetry, resulting in stronger horizontal shock. These results are similar to and as good as those obtained by a finite volume method on quadrilateral grids (see [13]).

4.6. *Orszag–Tang Vortex Test*

For the last test problem, the evolution of the Orszag–Tang vortex system described by Picone and Dahlburg [33] was considered. This problem simulates the MHD turbulence and offers the investigation of quickly evolving compressible turbulence starting from simple initial solutions. It is noted that the resistivity and viscosity used in [33] are totally determined by the dissipation mechanism of the model MHD-A.

The initial conditions have a periodic structure and involve x points (where the fields vanish) in both the velocity and magnetic field. Uniform initial density (ρ_0) and pressure (P_0) based on an average Mach number ($\equiv V/a$) and plasma beta ($= P/B^2/8\pi$) were selected, and periodic boundary conditions are assumed in both x and y directions. Note that one must be careful in applying these conditions since all possible updates at the boundary points should be taken into account very carefully before advancing to the next time level (for example, the node in one corner is affected by the cells adjacent to the other corners). The initial fields are produced as follows. First, the average velocity and magnetic fields (i.e., $\bar{V}_0^2 = \sum_{i=1}^{N}[V_x^2 + V_y^2]$ and $\bar{B}_0^2 = \sum_{i=1}^{N}[B_x^2 + B_y^2]$) are evaluated from the initial

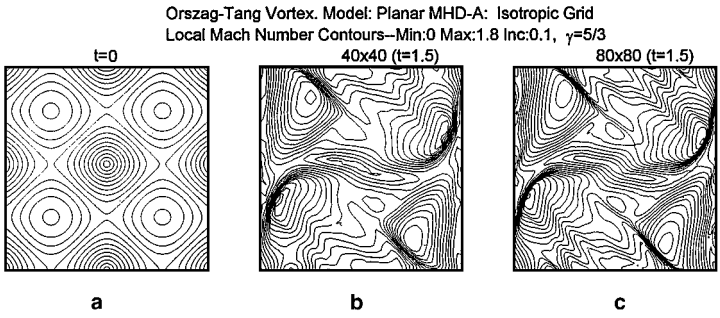

FIG. 7. Mach number contours obtained by the scheme described by Eq. (36) for the Orszag–Tang vortex test with the magnetic monopole wave obtained on 40×40 and 80×80 mesh.

fields:

$$\mathbf{V} = -\sin(2\pi y)\hat{i} + \sin(2\pi x)\hat{j}, \qquad \mathbf{B} = -\sqrt{4\pi}\sin(2\pi y)\hat{i} + \sqrt{4\pi}\sin(4\pi x)\hat{j}; \tag{88}$$

then ρ_0 and P_0 are evaluated from $\rho_0 = \gamma P_0(M^2/\bar{V}_0^2)$, $P_0 = \beta/(\bar{B}_0^2/8\pi)$ to be used as the initial values of the density and pressure. With this choice of initial conditions a wide variety of initial conditions can be produced. In this paper, the case $\beta = 10/3$ and $M = 1.0$ was examined on 40×40 and 80×80 isotropic triangular grids with $x, y : [0, 1]$ and $\gamma = 5/3$. The contours of local Mach number at $t = 0$ and $t = 1.5$ obtained by the same procedure are presented in Figs. 7a, and 7b and c respectively. As seen, the results show excellent symmetry and are similar to those obtained by Dahlburg and Picone, who used physical resistivity and viscosity. This suggests that the numerical dissipation built into the model presented here provides a good representation of the physical diffusive processes. The results show that the code is also capable of handling the x points where the flow is almost stationary or the magnetic field is negligible. The runs at later times show that the accuracy is degraded at subsonic part of flow (near center). This can be improved by using preconditioning, implicit time stepping, or hyperbolic–elliptic splitting techniques.

During the simulations presented thus far, the behaviour of $\vec{\nabla} \cdot \mathbf{B}$ was also monitored. This term was calculated numerically from

$$\epsilon = \left(\sum_{\text{mesh}} |\vec{\nabla} \cdot \mathbf{B}| \right) \left(\sum_{\text{mesh}} \frac{|B_x|_{\min} + |B_y|_{\min}}{\Delta x_{\max} + \Delta y_{\max}} \right)^{-1}, \tag{89}$$

as done by Evans *et al.* [32]. In particular, it was found in most of the tests that the numerical magnetic monopole wave (with the divergence source) has the stabilization effects against the discretization errors of the divergence condition although the problems are not eliminated completely. This is clearly seen from Fig. 8 (obtained from the Orszag–Tang vortex test) since the relative divergence error reduces almost linearly with the increased grid resolution (i.e., ϵ reduces approximately three times as the cell resolution is increased from 20×20 to 80×80). It is also seen that the divergence errors always reduce by the end of all iterations (which are stopped at $t = 1.5$). The curve at the top of Fig. 8 shows the increase in the time rate of divergence error when the magnetic monopole wave and the divergence source are not utilized. This phenomenon drives the creation of spurious magnetic monopoles, resulting in nonphysical dynamics. These numerical results also support the need for the numerical magnetic monopole wave in order to correctly update the magnetic field in such a way that the $\nabla \cdot \mathbf{B} = 0$ condition is satisfied to within the truncation errors in the solution.

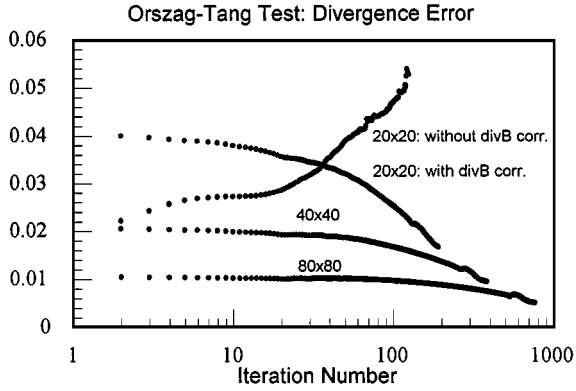

FIG. 8. The behaviour of the divergence error obtained with different grid resolutions for the Orszag–Tang vortex test with and without the magnetic monopole wave.

It seems that, in solving MHD equations, the divergence source and magnetic monopole wave can be efficiently utilized within the finite difference schemes (see [13–15]) with quadrilateral cells and fluctuation splitting schemes with triangular cells [18], although the divergence source occasionally introduces too small dissipations and it can be neglected for most cases.

4.7. *Behaviour of Model MHD-A on Unstructured Meshes*

The effects of unstructured grid and grid distortion are investigated by performing the author's contact discontinuity test on coarse and fine unstructured meshes and on a severely distorted mesh. The unstructured meshes were generated using the frontal Delaunay triangulation method of Muller [37], by specifying equally spaced points on the boundaries of the solution domain.

In order to compare the results of this test problem with the results obtained on unstructured meshes, the former was solved on a coarse isotropic mesh. The resulting density contour along with the isotropic mesh used and the time history of the maximum divergence error are shown in Fig. 9.

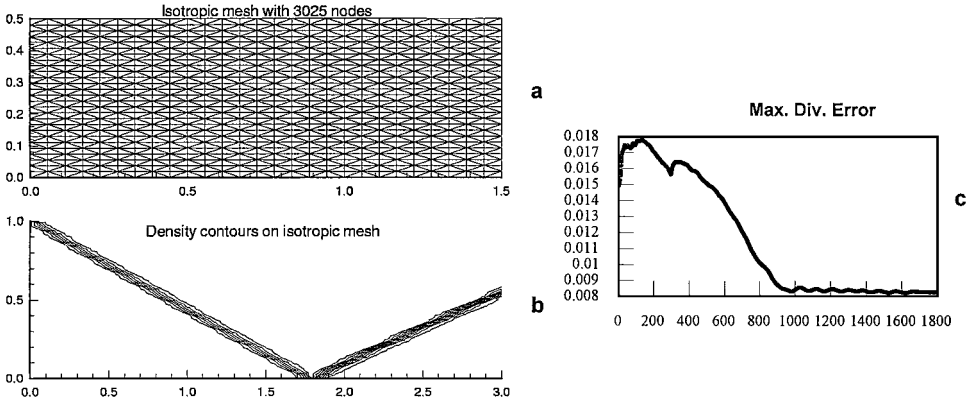

FIG. 9. The behaviour of model MHD-A on a coarse isotropic structured mesh: (a) isotropic mesh structure; (b) resulting density contour; (c) time history of maximum divergence error.

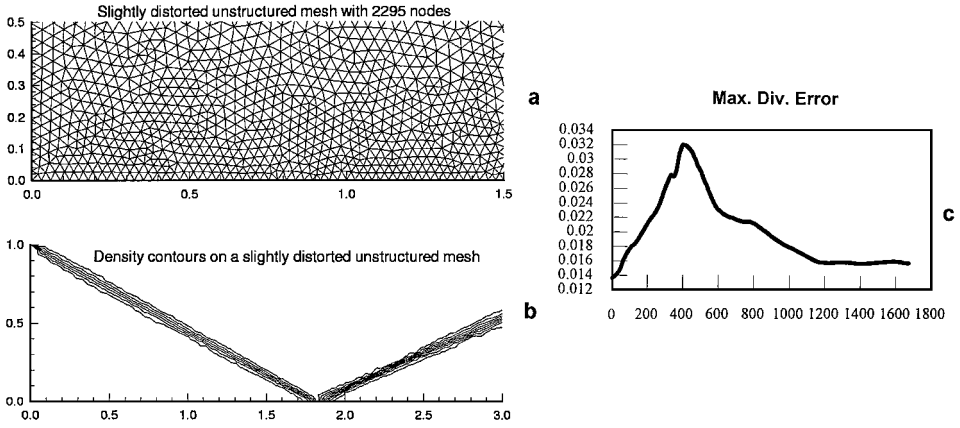

FIG. 10. The behaviour of model MHD-A on a coarse and slightly distorted unstructured mesh: (a) mesh structure; (b) resulting density contour; (c) time history of maximum divergence error.

Figure 10 shows the results obtained on a coarse and slightly distorted unstructured mesh (including approximately the same number of nodes existing in the isotropic mesh shown in Fig. 9). Comparing the resulting density contour with that of Fig. 9 one can see the success of the method on unstructured meshes. In addition, the time history of maximum divergence error is depicted in Fig. 10c. As seen, the divergence error reduces in time also for this case, showing the ability of model MHD-A to work accurately on unstructured meshes.

Figure 11 shows the results obtained on a severely distorted unstructured mesh. It is seen that the scheme developed here also works reasonably well on highly distorted unstructured meshes. The divergence error also reduces in time, although the convergence takes longer.

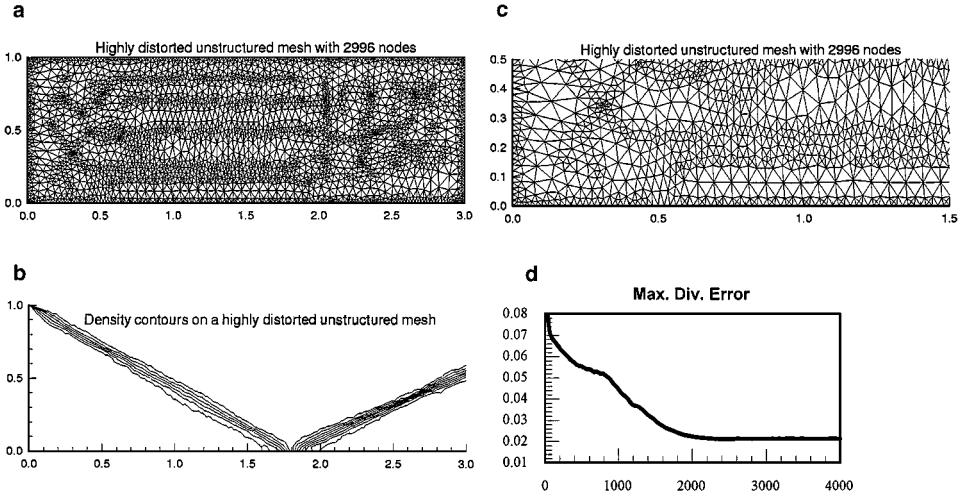

FIG. 11. The behaviour of model MHD-A on a severely distorted unstructured mesh for the author's contact discontinuity test: (a) mesh structure; (b) resulting density contour; (c) close-up illustrating the skewness of the elements used; (d) time history of maximum divergence error.

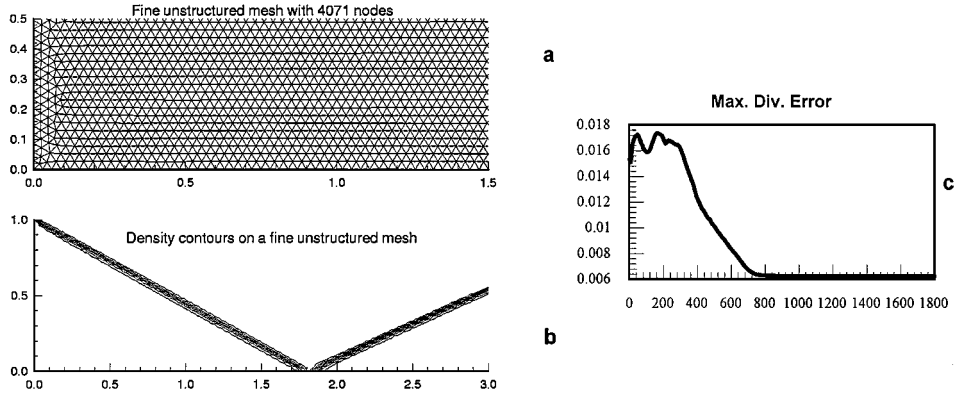

FIG. 12. The behaviour of model MHD-A on a fine unstructured mesh for the author's contact discontinuity test: (a) mesh structure; (b) resulting density contour; (c) time history of maximum divergence error.

In order to show the accuracy of the scheme on unstructured meshes, the same problem was solved on a finer unstructured mesh. The mesh structure and the resulting density contour along with the divergence error history are shown in Fig. 12. As seen, the result is excellent since the resolution is increased and the maximum divergence error is reduced considerably. All these results presented in this section show that the method presented in this paper is able to maintain the planarity of a plane discontinuity on nonuniform (even distorted) triangular meshes.

5. CONCLUSION

In this paper, a new fluctuation splitting wave model, MHD-A, for the solutions of planar MHD equations was presented. The model has a 10-wave structure consisting of an entropy. A new numerical magnetic monopole wave, and a pair of slow and fast magnetoacoustic waves and their counterparts moving in perpendicular direction. It was found that the magnetic monopole wave has a strength equal to the divergence of the magnetic field and that the magnetoacoustic waves propagate in the directions of maximum and minimum magnetic strain rates. The fluctuation splitting scheme, which includes the wave model MHD-A, was described in detail, and some numerical results for the scalar case and for MHD equations (Zachary's sonic test, author's contact and blast wave test problems, and Orszag–Tang vortex problem) were presented. The results show that the FS wave model MHD-A is a robust and efficient model for the solutions of planar MHD equations with arbitrarily oriented magnetic fields. No divergence cleaning and similar modifications are necessary to preserve the divergence free condition on the magnetic field. In addition, the method presented is able to maintain the planarity of a plane discontinuity on nonuniform triangular meshes.

ACKNOWLEDGMENTS

Partial supports from NATO Collaborative Studies Programme and NSF International with the University of Michigan are appreciated. The author also acknowledges Professors Terry Kammash and Phillip Roe for their continuous support, and the referees for their helpful comments on the final draft of this paper.

REFERENCES

1. N. Aslan, *Computational Investigations of Ideal MHD Plasmas with Discontinuities*, Ph.D. thesis, Nuclear Engineering Department, University of Michigan, 1993.
2. P. Colella and P. Woodward, The piecewise parabolic method (PPM) for gasdynamical simulations, *J. Comput. Phys.* **54**, 174 (1984).
3. S. Davis, A rotationally biased upwind difference scheme for the Euler equations, *J. Comput. Phys.* **56**, 65 (1984).
4. P. L. Roe, Discrete models for the numerical analysis of time-dependent multidimensional gas dynamics, *J. Comput. Phys.* **63**, 458 (1986).
5. A. Harten, B. E. Enquist, S. J. Osher, and S. R. Chakravarthy, Uniformly high order accurate essentially non-oscillatory schemes, III, *J. Comput. Phys.* **71**, 231 (1987).
6. M. Brio and C. C. Wu, An upwind differencing scheme for the equations of ideal magnetohydrodynamics, *J. Comput. Phys.* **75**, 400 (1988).
7. A. Zachary and P. Colella, A higher order Godunov method for the equations of ideal magnetohydrodynamics, *J. Comput. Phys.* **99**, 341 (1992).
8. P. R. Woodward and W. Dai, Extension of piecewise-parabolic method to multidimensional ideal magnetohydrodynamics, *J. Comput. Phys.* **115**, 485 (1994).
9. N. Aslan and T. Kammash, A new scheme for the numerical solutions of multidimensional MHD equations, in *ICASE/LaRC Workshop on Barriers and Challenges in CFD, Aug. 5–7, 1996, Hampton VA.*
10. N. Aslan and T. Kammash, A Riemann solver for two dimensional MHD equations, *Int. J. Numer. Methods Fluids* **25**, 1 (1997).
11. N. Aslan, Numerical solutions of one-dimensional MHD equations by a fluctuation approach, *Int. J. Numer. Methods Fluids* **22**, 569 (1996).
12. N. Aslan, Two dimensional solutions of MHD equations with an adapted Roe method, *Int. J. Numer. Methods Fluids* **23**, 1211 (1996).
13. N. Aslan and T. Kammash, Numerical fluxes with new sonic fix for MHD equations, *J. Comput. Phys.* **133**, 43 (1997).
14. K. G. Powell, *An Approximate Riemann Solver for Magnetohydrodynamics (That Works in More Than One Dimension)*, ICASE Report 94-24, Langley, VA, 1994.
15. T. I. Gombosi, K. G. Powell, and D. De Zeeuw, Axisymmetric modelling of cometary mass loading on an adaptively refined grid, *J. Geophys. Res.* **99**, 21525 (1994).
16. P. L. Roe and D. S. Balsara, Notes on the eigensystem of magnetohydrodynamics, *SIAM J. Appl. Math.* **56**, 57 (1996).
17. D. Ryu and T. W. Jones, Numerical magnetohydrodynamics: Algorithm and tests for one-dimensional flow, *Astrophys. J.* **442**, 228 (1995).
18. N. Aslan, MHD-A: A new wave model for magnetohydrodynamics equations, in *Godunov Symposium, May 1–2, 1997, University of Michigan, Ann Arbor*.
19. J. U. Brackbill and D. C. Barnes, The effect of nonzero $\vec{\nabla} \cdot \mathbf{B}$ on the numerical solution of the magnetohydrodynamic equations, *J. Comput. Phys.* **35**, 426 (1980).
20. J. D. Jackson, *Classical Electrodynamics*, 2nd ed. (Wiley, New York, 1975).
21. L. M. Mesaros, *Multidimensional Fluctuation Splitting Schemes for the Euler Equations on Unstructured Grids*, Ph.D. thesis, Aerospace Engineering Department, University of Michigan, 1995.
22. N. Aslan and T. Kammash, Plasma dynamics in a magnetically insulated target for inertial fusion, *Fusion Technol.* **26**, 184 (1994).
23. P. L. Roe, Approximate Riemann solvers, parameter vectors and difference schemes, *J. Comput. Phys.* **43**, 357 (1981).
24. H. Paillere, J.-C. Carette, and H. Deconinck, *Multidimensional Upwind and SUPG Methods for the Solution of the Compressible Flow Equations on Unstructured Grids*, von Karman Institute Lecture Series, 1994.
25. T. J. R. Hughes, M. Mallet, and A. Mizukami, A new finite element formulation for computational fluid dynamics. II. Beyond SUPG, *Comput. Methods Appl. Mech. Eng. Fluids B* **84** (1986).

26. D. Sidilkover and P. L. Roe, *Unification of Some Advection Schemes in Two Dimensions*, Tech. Report 95-10, ICASE, 1995.
27. B. Perthame, Convergence of N scheme for linear advection equations, in *Proceedings, SIAMM'94 Conference Lisbon* (J. Rodriguez, Ed.), ICASE, 1994.
28. P. L. Roe, Discrete models for the numerical analysis of time-dependent multidimensional gas dynamics, *J. Comput. Phys.* **63**, 458 (1986).
29. T. Linde, Modeling of the global helisphere, in *Godunov Symposium, May 1–2, 1997*, University of Michigan, Ann Arbor.
30. M. Rudgyard, *Multidimensional Wave Decomposition for the Euler Equations*, von Karman Institute Lecture Series, 1993.
31. A. Jeffrey and T. Tanuiti, *Non-linear Wave Propagation* (Academic Press, New York/London, 1964).
32. C. R. Evans and J. F. Hawley, Simulation of Magnetohydrodynamic flows: A constrained transport method, *Astrophys. J.* **332**, 659 (1988).
33. R. B. Dahlburg and J. M. Picone, Evolution of the Orszag–Tang vortex system in a compressible medium, *Phys. Fluids B* **1**, 2153 (1989).
34. S. A. E. G. Falle, S. S. Komissarov, and P. Joarder, A multidimensional upwind scheme for magnetohydrodynamics, *Mon. Not. R. Astron. Soc.* **297**, 265 (1998).
35. A. Hujeirat, IRMHD: An implicit radiative and magnetohydrodynamical solver for self-gravitating systems, *Mon. Not. R. Astron. Soc.* **298**, 310 (1998).
36. T. Tanaka, Finite volume TVD scheme on an unstructured grid system for three-dimensional MHD simulation of inhomogeneous systems including strong background potential fields, *J. Comput. Phys.* **111**, 381 (1994).
37. J.-D. Müller, *The Advancing Front Method and the Delaunay Triangulation: A Review with a Look at Data Structures, Vertex Generation and Grid Quality*, von Karman Institute Lecture Series, VKI LS 1994-02, Grid Generation, Belgium, 1994.